Available online at www.sciencedirect.com
SCIENCE DIRECT®
Icarus 181 (2006) 26–51
ICARUS
www.elsevier.com/locate/icarus

Light-toned layered deposits in Juventae Chasma, Mars

David C. Catling [a,b,*], Stephen E. Wood [a], Conway Leovy [a,c], David R. Montgomery [c], Harvey M. Greenberg [c], Christopher R. Glein [a], Jeffrey M. Moore [d]

[a] *Department of Atmospheric Sciences and Astrobiology Program, University of Washington, Box 351640, Seattle, WA 98195, USA*
[b] *Department of Earth Sciences, University of Bristol, Wills Memorial Building, Queen's Road, Bristol, BS8 1RJ, UK*
[c] *Department of Earth and Space Sciences, University of Washington, Box 351310, Seattle, WA 98195, USA*
[d] *Space Science Division, NASA Ames Research Center, MS 245-3, Moffett Field, CA 94035, USA*

Received 16 February 2005; revised 4 October 2005

Available online 27 December 2005

Abstract

We examine hypotheses for the formation of light-toned layered deposits in Juventae Chasma using a combination of data from Mars Global Surveyor's Mars Orbiter Camera (MOC), Mars Orbiter Laser Altimeter (MOLA), and Thermal Emission Spectrometer (TES), as well as Mars Odyssey's Thermal Emission Imaging System (THEMIS). We divide Juventae Chasma into geomorphic units of (i) chasm wall rock, (ii) heavily cratered hummocky terrain, (iii) a mobile and largely crater-free sand sheet on the chasm floor, (iv) light-toned layered outcrop (LLO) material, and (v) chaotic terrain. Using surface temperatures derived from THEMIS infrared data and slopes from MOLA, we derive maps of thermal inertia, which are consistent with the geomorphic units that we identify. LLO thermal inertias range from ∼400 to 850 $\mathrm{J\,m^{-2}\,K^{-1}\,s^{-1/2}}$. Light-toned layered outcrops are distributed over a remarkably wide elevation range (∼5.8 km) from the chasm floor to the adjacent plateau surface. Geomorphic features, the absence of small craters, and high thermal inertia show that the LLOs are composed of sedimentary rock that is eroding relatively rapidly in the present epoch. We also present evidence for exhumation of LLO material from the west wall of the chasm, within chaotic and hummocky terrains, and within a small depression in the adjacent plateau. The data imply that at least some of the LLO material was deposited long before the adjacent Hesperian plateau basalts, and that Juventae Chasma underwent, and may still be undergoing, enlargement along its west wall due to wall rock collapse, chaotic terrain evolution, and exposure and removal of LLO material. The new data allow us to reassess possible origins of the LLOs. Gypsum, one of the minerals reported elsewhere as found in Juventae Chasma LLO material, forms only at low temperatures (<60 °C) and thus excludes a volcanic origin. Instead, the data are consistent with either multiple occurrences of lacustrine or airfall deposition over an extended period of time prior to emplacement of Hesperian lava flows on the plateau above the chasm.

Keywords: Mars; Mars, surface; Geological processes; Mineralogy; Infrared observations

1. Introduction

Layered deposits of relatively high albedo are commonly found on the floors of large craters and deep chasms in the martian tropics and subtropics, including the Valles Marineris canyon system. Such light-toned deposits were first identified in Mariner 9 images in Valles Marineris chasms as large mounds or mesas that appeared layered in the interior of the canyons (Sharp, 1973; McCauley, 1978). The original light–dark layering identified in the deposits from Mariner 9 was misleading, however. Images from the Mars Orbiter Camera (MOC) on Mars Global Surveyor (MGS) show that dark bands identified in Mariner 9 images are really areas mantled by dark, eroded debris (Weitz et al., 2001; Malin and Edgett, 2001). MOC and the Thermal Emission Imaging System (THEMIS) on Mars Odyssey (MO) have revealed that the light-toned material is indeed layered but at a finer scale than could be seen in Mariner 9 images. The layered materials have commonly been called 'interior layered deposits' (ILDs). Similar light-toned sedimentary layers are also found in the inter-crater plains so that the more general non-genetic term 'light-toned layered outcrops' is used by Malin and Edgett (2001) for all such deposits. We adopt this term here, and abbreviate it to LLO.

* Corresponding author. Fax: +44 117 925 3385.
E-mail address: davidc@atmos.washington.edu (D.C. Catling).

0019-1035/$ – see front matter
doi:10.1016/j.icarus.2005.10.020

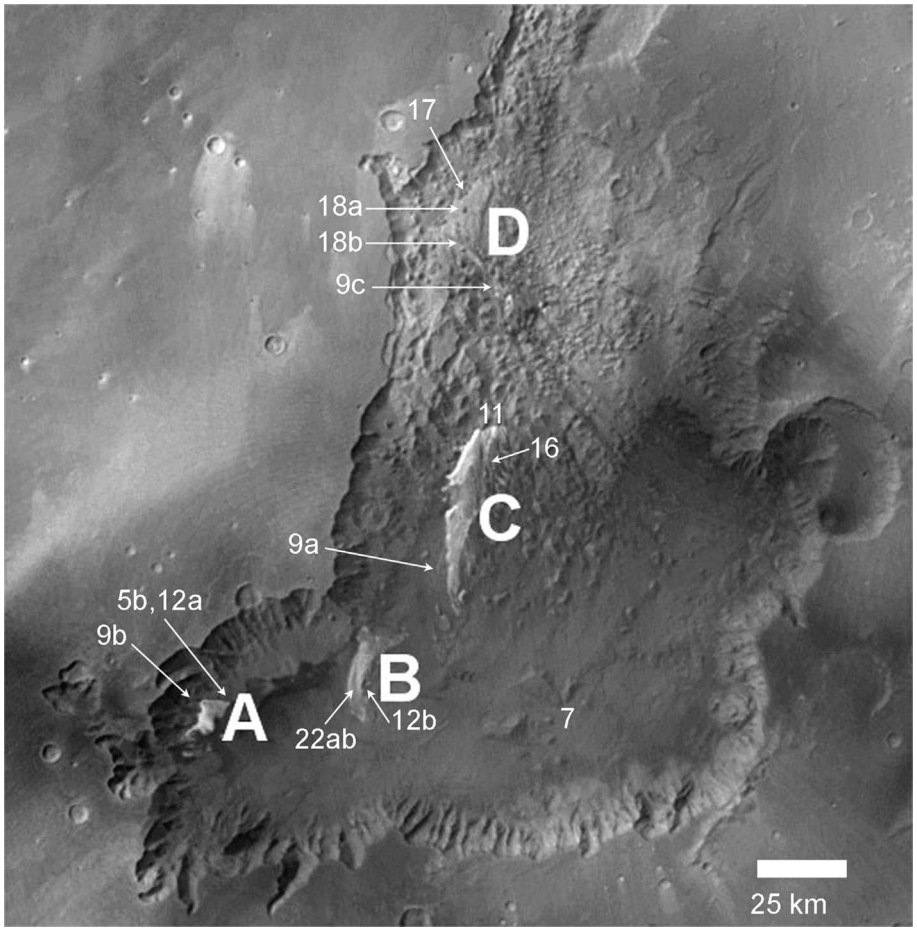

Fig. 1. Context mosaic of MOC wide-angle images showing Juventae Chasma. Outcrops of light-toned layered deposits are labeled 'A' through 'D' running south to north. Numbered arrows show the locations of images shown in other figures.

A variety of theories have been presented for the origin of LLOs in Valles Marineris and closed chasms in the surrounding region. The possible origins are: (1) lacustrine sedimentary deposits formed either within the chasm or prior to its development (McCauley, 1978; Nedell et al., 1987; Komatsu et al., 1993; Malin and Edgett, 2000b) that have been hypothesized to be of carbonate composition (McKay and Nedell, 1988; Spencer and Fanale, 1990); (2) remnants of wall rock material (Malin, 1976); (3) mass wasted materials from the walls (Nedell et al., 1987; Lucchitta et al., 1994); (4) aeolian deposits (Peterson, 1981; Nedell et al., 1987; Malin and Edgett, 2000b); and (5) volcanic deposits (Peterson, 1981; Lucchitta et al., 1994; Chapman et al., 2003; Komatsu et al., 2004).

For this paper, we focus on LLOs in one particular chasm, Juventae Chasma, a deep closed depression centered near 4° S, 61° W and approximately 500 km north of Valles Marineris. The lowest point of the floor of Juventae Chasma lies 4.4 km below the topographic datum (Section 3), as defined by the Mars Orbiter Laser Altimeter (MOLA) on the MGS spacecraft (Smith et al., 2001), and 6–7 km below a surrounding, sloping plateau of Hesperian age (Fig. 1) (Hartmann and Neukum, 2001). The chasm is of particular interest because it is situated at the southern end of a northward flowing 50–150 km wide outflow channel, Maja Vallis (Baker and Kochel, 1979). The immediate source region for Maja is chaotic terrain that covers much of the northern part of Juventae Chasma. Chapman et al. (2003) previously described three large (>50 km^2) LLOs south of the chaos region close to the foot of the western wall of the chasm labeled 'A' to 'C' in Fig. 1. New data allow us to assess the geomorphologic context and thermophysical properties of the LLOs in more detail. Using a combination of data from instruments on MGS (MOC, MOLA (Smith et al., 2001), and the Thermal Emission Spectrometer (TES) (Christensen et al., 1998)), as well as THEMIS data (Christensen et al., 2004), we characterized the three LLOs of Chapman et al. (2003) and a fourth LLO ('D' in Fig. 1). We also identified the locations of numerous smaller outliers of LLO material across a much greater areal extent than previously known. MOC and THEMIS images have also allowed us to characterize the erosional styles of the LLO surfaces, and we compare their differences and similarities. Furthermore, we present new maps of the thermal inertia of the LLOs and surrounding terrain derived from THEMIS data. These maps place thermophysical constraints on the possible nature of the deposits and allow some material identification that cannot be done purely with images. The combination of thermal inertia, geomorphology and lack of small craters suggest that the LLOs are composed of sedimentary

rock that is undergoing active retreat by abrasion and deflation.

Understanding the nature of the LLOs in Juventae Chasma is likely to provide insight into the evolution of Mars, as the physical relationships between chasms, LLOs, chaos, and outflow channels remain to be clearly elucidated. The association of chaos regions with outflow channels motivated the widely held hypothesis that one or more sudden releases of groundwater or melt water from sub-surface ice eroded outflow channels (Sharp, 1973). However, the floor of Juventae Chasma lies topographically below the southernmost streamlines of Maja Vallis, as noted by (Chapman et al., 2003). We locate a "pour point" north of Juventae Chasma at the 509 m MOLA contour (Section 3) and investigate whether the LLOs are ancient remnant material associated with the formation of the chaos or whether the LLOs are superposed deposits that formed within the chasm in a more recent epoch (Sections 3–5). Recent near-infrared spectral data from the OMEGA instrument on board the Mars Express (ME) spacecraft shows that LLO 'B' is rich in hydrous sulfates, with a gypsum ($CaSO_4{\cdot}2H_2O$) signature on its west side and top and kieserite ($MgSO_4{\cdot}H_2O$) signature on its lower east side (Bibring et al., 2005; Gendrin et al., 2005). Thus, we also consider the geochemical composition with respect to the origin of the LLO material and implications for associated chaos and outflow channels.

2. Use of THEMIS data

Before discussing Juventae Chasma and its LLOs in detail, we begin by describing our use of THEMIS data to derive thermal inertia (TI). In all subsequent sections, we use thermal inertia (TI) derived from THEMIS data to help us interpret the geomorphology seen in MOC images. For example, TI allows us to distinguish whether the LLOs are sedimentary rocks versus indurated dust deposits, such as "White Rock" (Ruff et al., 2001), which cannot be done with images alone; we also use TI to deduce whether some geomorphic units are sand or dust covered. Previously published TI maps derived from TES (Mellon et al., 2000) are too poor in spatial resolution to significantly aid the interpretation of MOC narrow angle (NA) images of the LLOs. The horizontal resolution of the TES-based TI maps is 3 km, and their derivation uses a TES albedo map with has a resolution of 15 km. LLO 'A' in Juventae Chasma (Fig. 1) is only ∼5 km across and is obviously not resolved by TES TI; the other LLOs are also poorly resolved with TES TI. Mellon et al. (2000) also assume that the surface is flat in their derivation of TI—obviously an invalid assumption for LLOs.

In order to provide TI data that can be used to analyze the nature of LLOs and their surroundings, we have developed a method to derive ∼100 m pixel^{-1} TI maps from THEMIS infrared data that uses MOLA topography to account for the slope and azimuth of the landscape. This method is described in detail in Appendix A.

3. Geologic setting of light-toned layered formations in Juventae Chasma

3.1. Topographic context

Juventae Chasma is ∼185 km across at it widest point in its southern portion, and ∼270 km long in the north–south direction (Fig. 2). The lowest point (61.29° W, 4.75° S) lies at an elevation of −4.4 km within an ∼18-km-diameter bowl-shaped depression in the southeast portion of the chasm, perhaps indicative of an impact crater. (All elevations given in this paper are those in the 1/128° map of gridded data from MOLA.) The whole chasm is surrounded by plains that slope downward to the northwest from about 2.6 km elevation at the southwest corner of Juventae to 1.4 km elevation at the north end of the chasm. Chapman et al. (2003) noted that the floor of Juventae lies below the opening of Maja Vallis outflow channel, which like the other outflow channels has been suggested to have been carved by floodwaters (Komar, 1979; Baker and Kochel, 1979). Consequently, the topographic barrier to flow from the south would require either ponding of water within Juventae Chasma or concurrent incision of the upper chasm followed by continued excavation or collapse. Using the topography of Mars in the current epoch with the Geographic Information System (GIS) Arcinfo, we found that water would fill Juventae Chasma up to an elevation of 509 m. This elevation represents a pour point into Maja Vallis to the north of the chasm, as shown in Fig. 3.

3.2. Geology of Juventae Chasma

We divide Juventae Chasma into geomorphic units of (i) chasm wall rock, (ii) heavily cratered hummocky terrain, (iii) a mobile and largely crater-free sand sheet on the chasm floor, (iv) light-toned layered outcrop (LLO) material, and (v) chaotic terrain.

3.2.1. Geologic map

Fig. 4 shows the geomorphic units that we mapped in Juventae Chasma, while Table 1 shows THEMIS-derived thermal inertia values for these geomorphic units that help form the basis for our geomorphic map. The most detailed geologic map prior to MGS and MO data was that produced by Lucchitta et al. (1994). However, THEMIS and MOC images allow us to distinguish units with more accurate placement of boundaries (Fig. 5a). MOC images and thermal inertia calculations show that Lucchitta et al.'s (1994) "dark material" unit is mobile dark sand that we lump into a single sand sheet; indeed, in places this dark unit blends seamlessly into the sand sheet (e.g., the southern portion of MOC NA image E1201685). Consequently, although the dark material may be a lithologically distinct unit, we designate this dark unit part of the sand sheet depositional unit rather than a separate entity. However, we note that in other places, this dark sand clearly superposes other sand that is somewhat higher in albedo (arrow 1 in Fig. 5b). The sand sheet is also seen to contact and partly overlie the boundaries of LLO 'A' and to define a contact with the base of Juventae's west

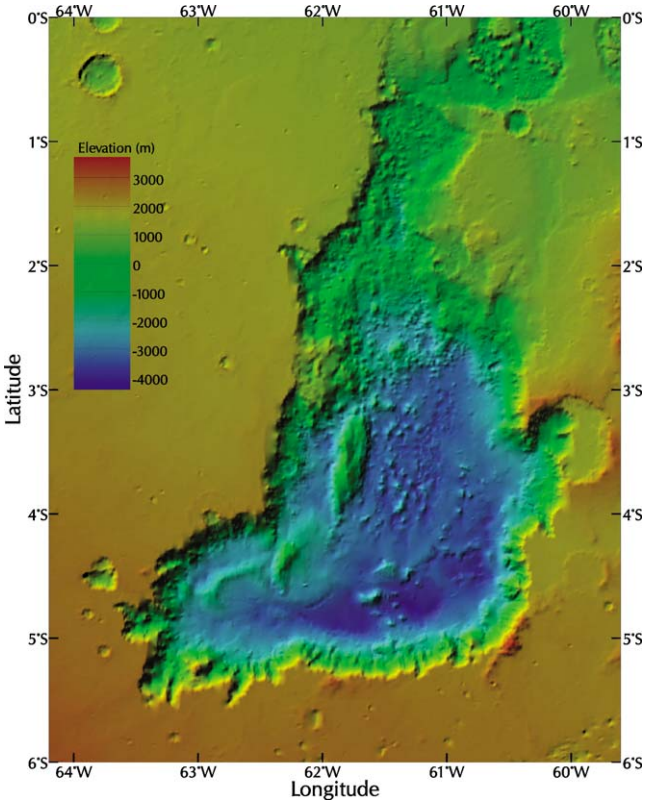

Fig. 2. A topographic map of Juventae Chasma, constructed using 1/128° Mars Orbiter Laser Altimeter (MOLA) data.

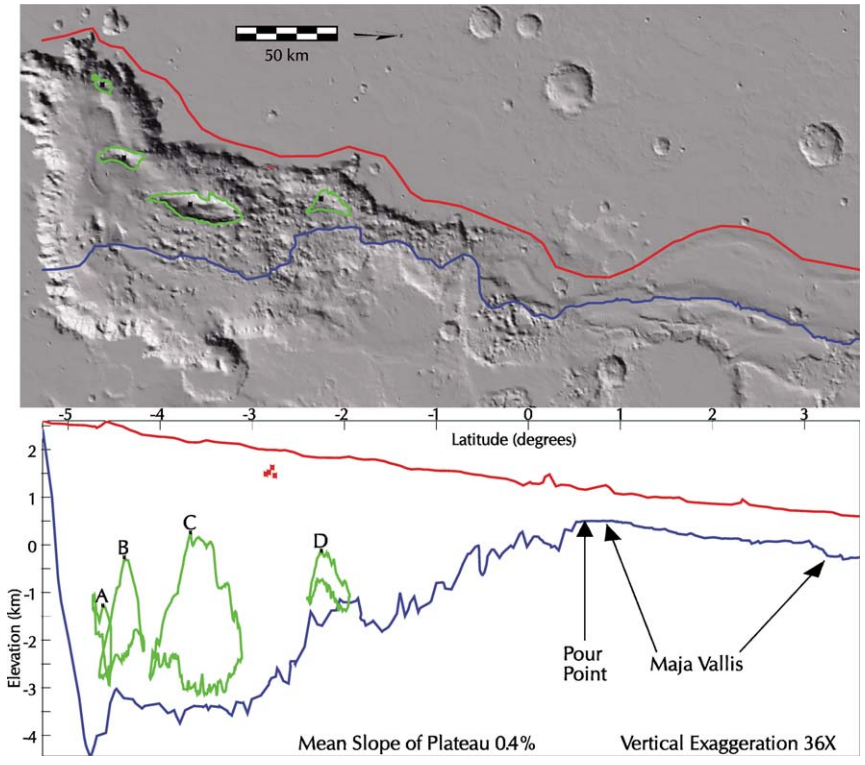

Fig. 3. (Upper panel) The blue line follows a path from the southern plateau through the lowest point of Juventae Chasma and through the "pour point" marked in the lower panel. The red line is an arbitrary path to indicate the relative elevation of the plateau. Green lines mark the boundaries of the four major LLOs, 'A' to'D.' (Lower panel) A plot of elevation versus latitudinal distance. A "pour point" elevation of 509 m is marked by an arrow. Water would pour out from this level and follow the path of steepest descent along Maja Vallis to the north, following the blue line. The green lines mark the boundaries of LLOs 'A'–'D' and their highest points. Red squares at ~2.7° S mark the elevation of possible fluvial terraces on the upper wall of Juventae Chasma, which can be compared with the "pour point" elevation.

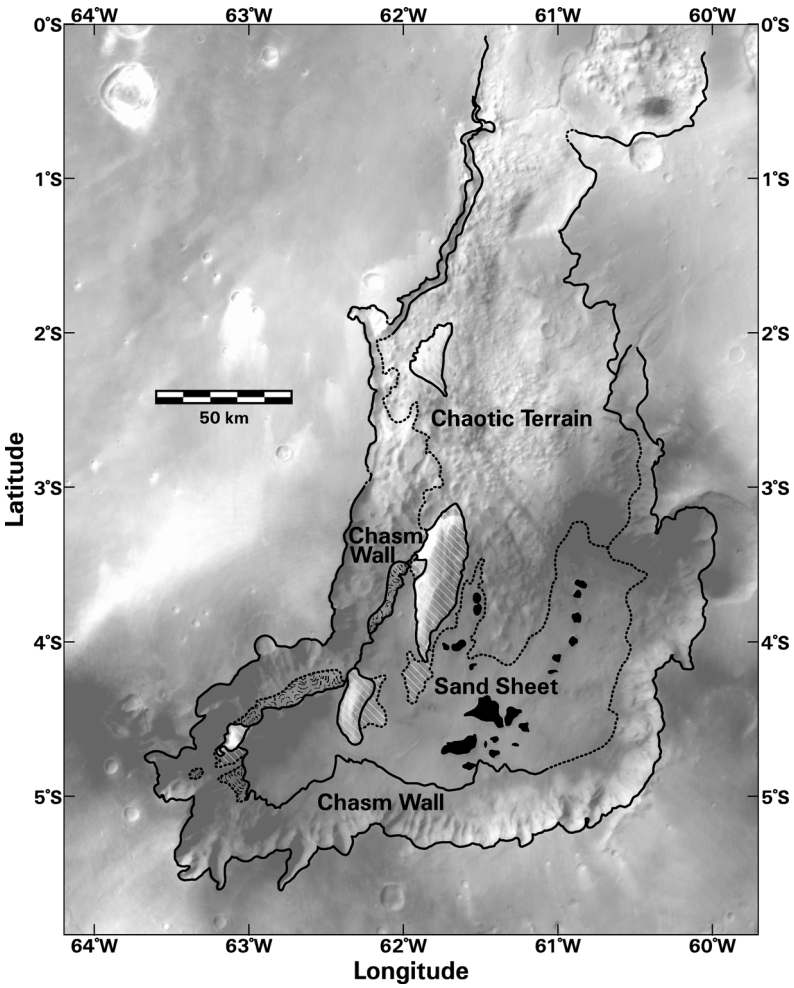

Fig. 4. We identify five geomorphic units within the chasm: (1) a sand sheet, (2) chaotic terrain, (3) light-toned layered outcrop (LLO) material (cross-hatched), (4) chasm wall material, and (5) hummocky terrain (stippled). Above the chasm is a Hesperian-age plateau. The four LLOs are bounded by solid lines, while dashed lines that enclose hatching indicate outcrops of LLO material, which we identify as probable extensions of the four main LLOs. Other dashed lines indicate inferred contacts between geomorphic units. Large chaotic, rocky blocks found within the sand sheet unit are indicated with solid black.

Table 1
Thermal inertia values for geological settings within Juventae Chasma

Juventae Chasma feature	Elevation (km)	Best-fit thermal inertia ($J\,m^{-2}\,s^{-1/2}\,K^{-1}$)	Best-fit albedo (relative)	Interpretation
Plateau NW of LLO 'B'	+2.5	200–300	Dark	Fine sand
Plateau N of LLO 'A'	+2.6	500–600	Bright	Bedrock covered by thin layer of sand or dust
S. chasm floor material	−3.0	∼350	Very dark	Coarse-grained sand in sand sheet
Spur and gully landforms of walls	−2.5 to +2.5	350–1200+	–	Bedrock exposed on ridge-tops or covered by sand on slopes
Hummocky terrain	−3.0 to −2.8	600	Medium	Bedrock and LLO outcrops
Chaotic terrain cones	−2.5 to +1	400–600	Dark	Bedrock, with LLO outcrops and partial sand cover
LLO 'A'	−2.0 to −1.3	500–850	Very bright	Sedimentary rock covered by thin layer of dust w/ pockets of sand
LLO 'B'	−2.5 to −0.4	350–620	Bright	– „ –
LLO 'C'	−2.5 to +0.4	350–800	Bright	– „ –
LLO 'D'	−1.0 to 0.0	350–550	Medium	Sedimentary rock w/thick sand layer

wall. We now describe the various geologic units in turn, before giving a detailed description of the LLOs in Section 4.

3.2.1.1. Plateau The plateau that surrounds the chasm forms part of the northeastern flank of the Tharsis bulge and thus basaltic lava flows are believed to comprise its bulk. Numerous craters on the plateau suggest an Hesperian age, but are generally highly degraded by erosion and infilling. MOC images show that very small craters (<50 m diameter) are sparse. Low thermal inertia of typically ∼230 $J\,m^{-2}\,K^{-1}\,s^{-1/2}$ implies

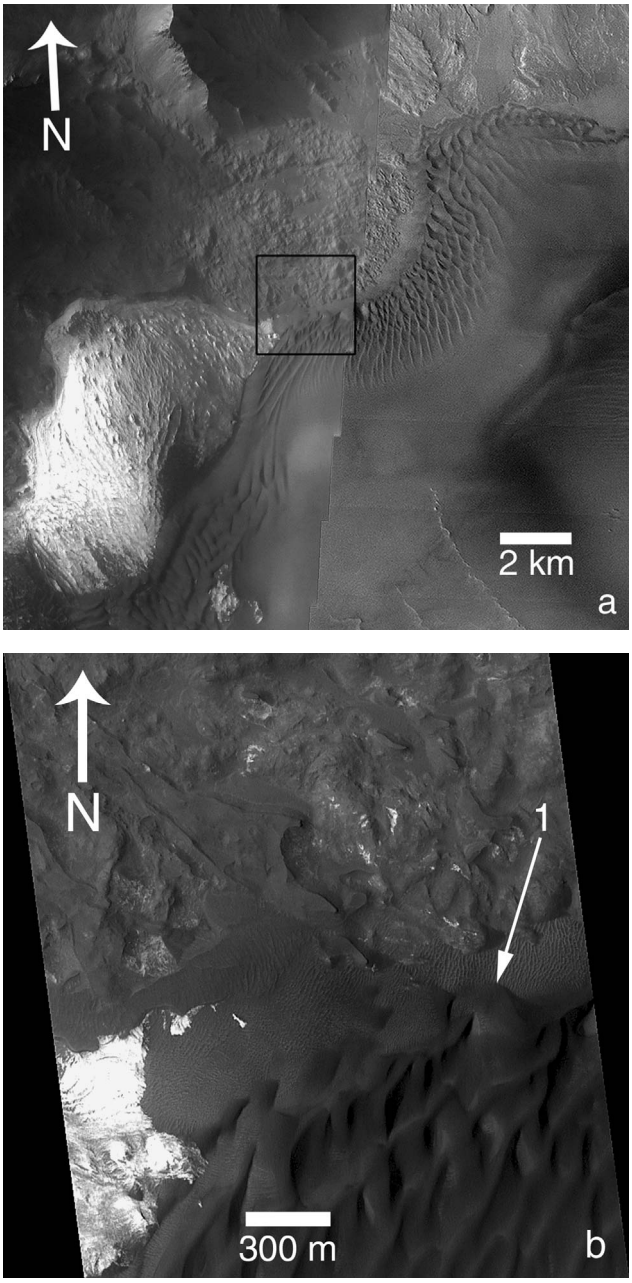

Fig. 5. (a) Context mosaic of THEMIS images V05558002 and V08529001. Inset shows Fig. 5b. (b) Zoomed portion of MOC image M030179 showing the contact of the sand sheet with hummocky terrain and the eastern portion of LLO 'A.' Also note the LLO outcrops in the hummocky terrain. An arrow shows the contact of the dark barchanoid dunes with a light-toned dune field.

that the plateau is mantled by at least centimeters of very fine (∼200 μm) sand or a sand/dust mixture (following the work of Presley and Christensen, 1997). Un-cemented dust-sized particles (<20 μm) on Mars could have a thermal inertia up to ∼170 $\mathrm{J\,m^{-2}\,K^{-1}\,s^{-1/2}}$ (Presley and Christensen, 1997), so another possible match to ∼230 $\mathrm{J\,m^{-2}\,K^{-1}\,s^{-1/2}}$ could be cemented dust.

3.2.1.2. Wall rock The descent into Juventae Chasma is typified by a steep face at the top of the wall, followed by ridges and troughs (so-called "spur and gully" landforms) that penetrate laterally and vertically into the chasm. MOC image sampling of the western chasm wall is relatively good and allows us to deduce a general wall stratigraphy. An uppermost rock unit descends approximately 1 km from the plateau in a steep multi-layered outcrop of dark material, where the typical thickness of individual layers is a few tens of meters (MOC NA images M1300038, M2000116, M2100902, and E1102581). Large blocks can be identified in portions of the upper wall and large boulders occur on the underlying slope (NA images M1102581, M1200299). The high thermal inertia of rocky material beneath the cliff top (600–1200+ $\mathrm{J\,m^{-2}\,K^{-1}\,s^{-1/2}}$) and the regional setting on the northeast edge of the Tharsis volcanic province are consistent with these cliffs consisting of bedrock from lava flows. However, directly beneath the upper wall unit is a steeply sloping surface consisting of rocky ridges and spurs separating steep talus-filled valleys with higher albedo than the upper rock unit (e.g., MOC NA images M1000466, M2000116, M1200299, M0401949, M0401951, M1300038, M2100902, and E110370). The high thermal inertia of the ridge and spur crests (Table 1) suggest that the ridges and spurs consist of bedrock underlying or derived from the upper wall formation. Infill in the valleys has an intermediate thermal inertia consistent with sand or a poorly graded mixture of fine and coarse material. Based on morphology, location and thermal inertia, we propose that the valley-filling material is scree. We further hypothesize that retreat and collapse of the cliff face may generate sand that over geological time has contributed to the dark sand sheet that stretches over the southern chasm floor (Fig. 4). Evidence of slumping can also be found adjacent to LLOs 'B' and 'C.'

We also identify apparent strath terraces along Juventae Chasma's upper wall, located at ∼62.2° W between 2.2 to 2.9° S (Fig. 6). (A strath is an erosional bedrock-cored terrace (Bucher, 1932).) The floor of these benches lies about 100–200 m below the cliff top. These possible fluvial strath terraces are located at about 1500 m elevation, roughly 1 km above the Maja ∼500 m pour point, which indicates that channels started forming either before or contemporaneous with Juventae Chasma itself. Although exhibiting arcuate lateral boundaries evocative of landslide morphology, these terraces are not landslides because the higher-elevation potential scarp features do not cut across lower elevation terraces. The lack of landslide deposits and morphology on the valley wall below the terraces reinforces our interpretation.

3.2.1.3. Hummocky terrain A hummocky unit with a high density of small craters lies along the base of the west wall (Fig. 5). This unit possesses intermediate albedo relative to surrounding units and on its upper slope grades into heavily cratered slides on the chasm wall. Going from south to north along the west wall, the following MOC NA images contain hummocky terrain: M2000116, R0300948, E1102581, R0200160, M0301709, M0201551, R0100978, M2301701. The hummocky unit is a few kilometers wide and where it is not covered with sand or dunes, the thermal inertia is relatively high ∼600–700 $\mathrm{J\,m^{-2}\,K^{-1}\,s^{-1/2}}$. Within the hummocky

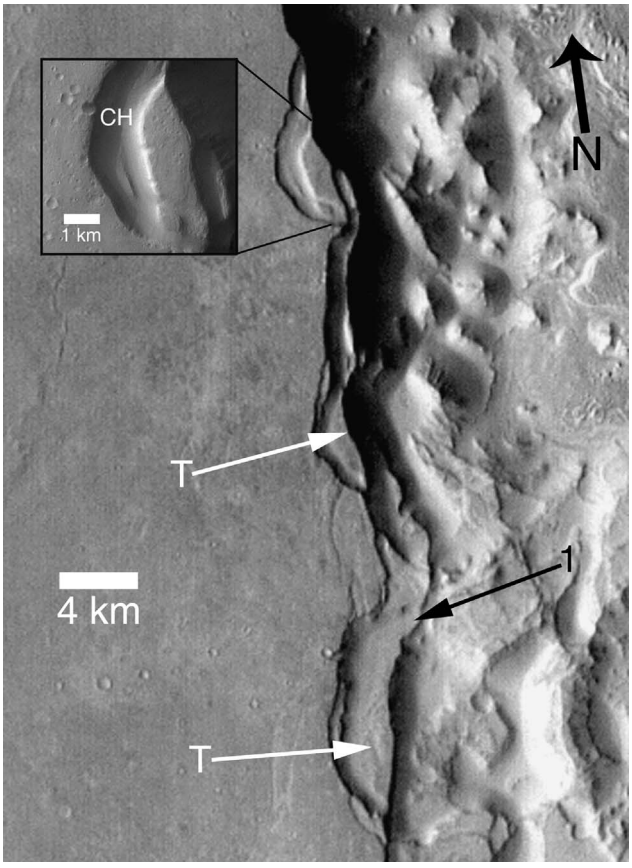

Fig. 6. Portion of THEMIS infrared image I01450007 showing apparent fluvial terraces (T) and channel (CH) incised into the upper wall of Juventae Chasma. The inset is from THEMIS visible image V11599001. Arrow 1 indicates a location where the terrace surface does not appear offset by an arcuate scarp (and potential landslide headscarp) incised into the edge of the Hesperian plateau.

unit, small outcrops of light-toned LLO material are sometimes apparent (Fig. 5). The lowest portion of the hummocky unit lies at an elevation of about −2.8 km. Hummocky terrain may be more extensive than mapped along the south wall in Fig. 4, but we are unable to confirm this possibility because of the limited number of high-resolution MOC images in that area.

3.2.1.4. Sand sheet A sand sheet forms the bulk of the southern chasm floor and has a low albedo of typically ∼0.15 based on TES bolometer data (Mellon et al., 2000). Dark dune forms are found adjacent to LLOs 'A'–'C,' including complex and barchanoid forms (MOC NA images M0003063, M0301709, M2300781, E1101370, E110370, and E1201685). Slip faces on barchanoid dunes in the western part of the sand sheet indicate that the controlling winds are from the NW to WNW (e.g., see Fig. 5b), which is the direction of downslope flow from the western wall of the chasm. To the east of the dark dunes, the chasm floor consists mainly of low-relief undulations that are almost entirely free of small impact craters and contain some aeolian bedforms (MOC NA images M0003063, M0303132, M0401950, M0802666, M1001391, M120170, and E110370). Occasional outcrops of bedrock are sometimes flanked on their

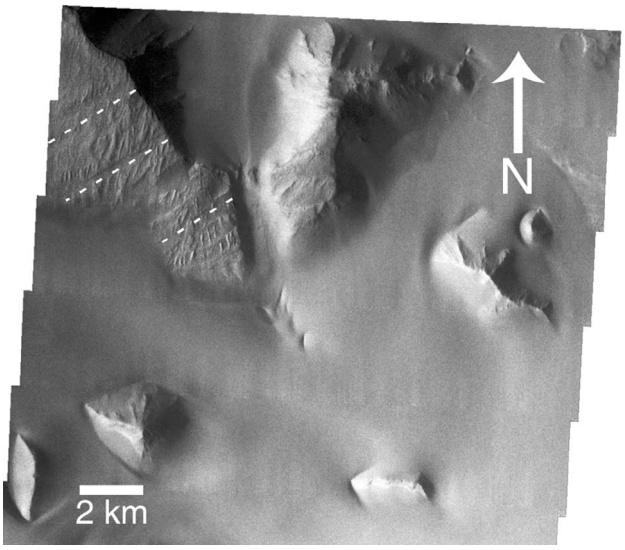

Fig. 7. A rocky block located in the sand sheet in southern Juventae Chasma. Note the dipping strata within the rocky block. (Portion of THEMIS visible image V09415002.)

NW side by streamlined undulations suggestive of flow deflection around the outcrop. The presence of dunes and an intermediate thermal inertia of typically ∼350–400 $\mathrm{J\,m^{-2}\,K^{-1}\,s^{-1/2}}$, suggest that the surface consists of coarse-grained sand (Presley and Christensen, 1997); ∼0.7 mm typical grain size would be consistent with the thermal inertia values (although finer sand that has undergone induration is an alternative). The dark sand sheet impinges upon the east side of LLOs 'A'–'C' and the hummocky unit at the base of the western wall (e.g., Fig. 5).

3.2.1.5. Chaotic terrain Classic chaotic terrain identified in Mariner and Viking images consists of lowlands filled with a jumble of large angular blocks and slump blocks adjacent to cratered uplands (Sharp, 1973). MOC images show greater detail, including kilometer-scale broken blocks, cones and plateaus separated by valleys and gullies filled with aeolian bedforms. In Juventae Chasma, chaotic terrain covers approximately the northern half of the chasm floor, bounded by the sand sheet and LLO 'C' at its southern edge (Fig. 4). Outcrops of LLO material are exposed within this chaotic unit, as described in the next section.

In the southern part of Juventae Chasma, within and partially buried by the sand sheet are large rocky blocks (colored black in Fig. 4). Fig. 7 shows how one of these large blocks has dipping strata, which resembles the layering seen in chasm walls. The block also has vertical erosional features that are tilted relative to the stratigraphic layers. This displaced ∼10 km block of chasm wall material is presently ∼30 km away from the nearest chasm wall to the south.

4. Characteristics of the light-toned layered outcrops

4.1. General occurrence and topography

Four major LLOs (area >50 $\mathrm{km^2}$) in Juventae Chasma (labeled 'A' through 'D' in Fig. 1) form prominent positive topo-

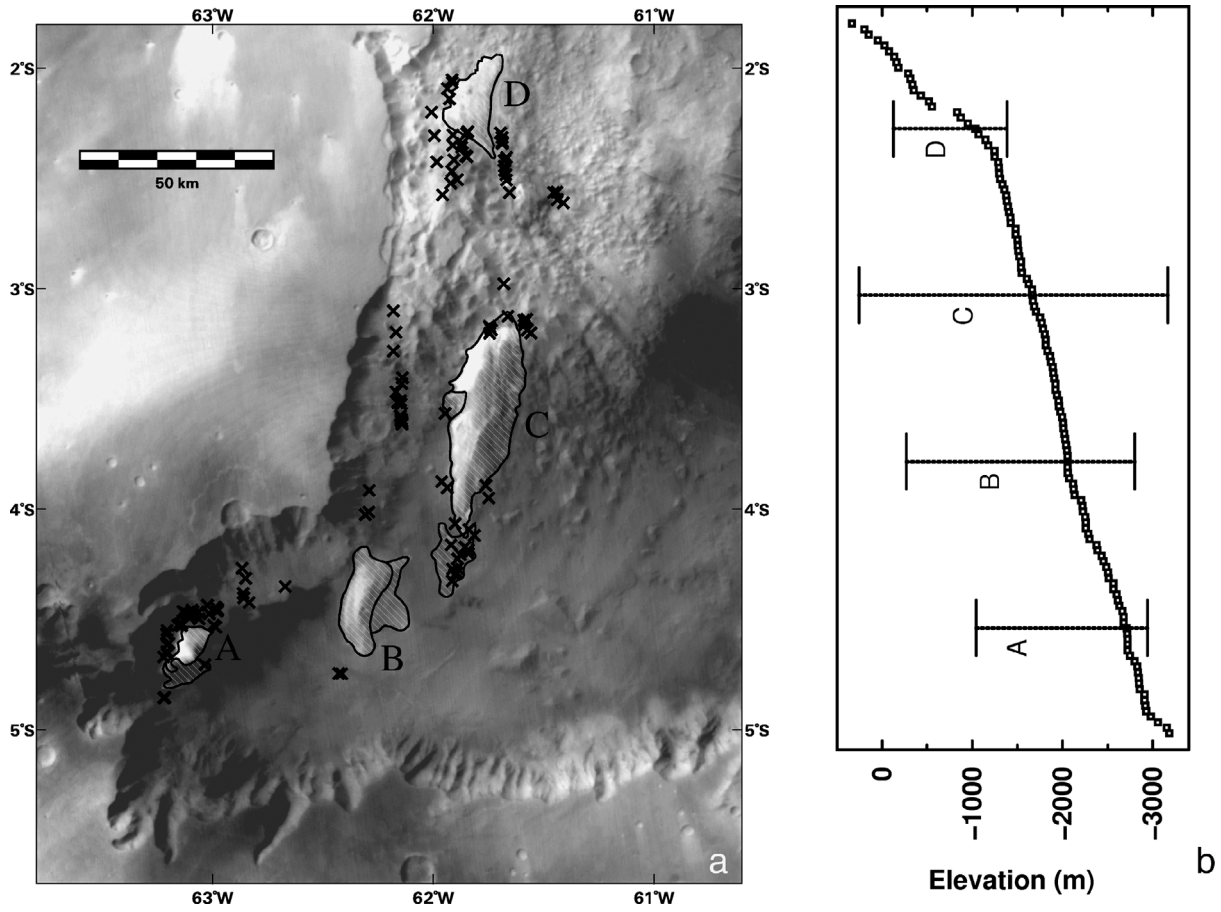

Fig. 8. (a) Location of light-toned layered deposit outliers marked with crosses. (b) The range in elevation of light-toned layered outliers compared to LLOs 'A'–'D.' The vertical range of LLOs 'A'–'D' are shown as vertical bars, where the lowest point is that on the boundary of each LLO unit shown in Fig. 4.

graphic features within the chasm. 'C' is the largest and tallest of these, ∼50 km long and ∼20 km wide. The summit of 'C,' at 257 m above the standard Mars datum, the highest point within the chasm, lies on a ridge at 61.80° W, 3.67° S (Fig. 3). Since the lowest base of 'C' lies at about −3 km, its total rise is ∼3.3 km from base to crest. Thus 'C' is comparable in size to small terrestrial mountain ranges, for example the Teton Range in northwest Wyoming, whose peak rises ∼2.1 km above its surrounding plain. LLO 'B' rises to a summit at −266 m (62.31° W, 4.62° S), ∼2.8 km above the chasm floor to its east. The highest point on the southwest tail of 'A' is −1042 m (63.2° W, 4.72° S), with a secondary peak at −1276 m (63.12° W, 4.62° S). There is a steep slope to hummocky terrain to the northeast and a shallower southwest slope to a depression centered at 63.15° W, 4.65° S (Fig. 2).

We have identified many outliers of LLO material in MOC NA images. The location and elevation range of these outliers compared to the major LLOs is shown in Figs. 8a and 8b, respectively; most are exposed on the chasm floor or wall slopes near the four prominent LLOs, or in the chaotic terrain north of LLO 'C.' Some apparent outliers are also found in hummocky terrain near the base of the west wall of the chasm (Fig. 5b). The strikingly continuous distribution of outlier elevations spans the full range of elevations of the exposed portions of LLOs 'A'–'D' (Fig. 8b). Outliers on the floor of the chasm tend to have low relief, and often have small craters on their surfaces, suggesting that they correspond to old LLOs whose surfaces have been protected from resurfacing following impact cratering (Fig. 9a). Outliers on the wall slopes often occur beneath rocky ridges (Fig. 9b). Outliers in chaotic terrain appear in conjunction with ridges, mounds, and plateaus (Fig. 9c).

The most surprising light-toned layered material is found in a small depression farther west of Juventae Chasma at an elevation of ∼0.8 km, and on the edge of the plateau to the west of Juventae Chasma (Fig. 10). This material superposes Hesperian lava flows that comprise the cliffs forming the walls of Juventae Chasma. Together with evidence for LLO exhumation (see below), the wide range of settings for light-toned layered material ranging from the top of the Hesperian plateau to the depths of Juventae Chasma may suggest multiple LLO formation events occurring over a long period extending well back into the Hesperian and possibly the Noachian. An alternative possibility, discussed in Section 6, is that the light-toned material within Juventae Chasma was formed by a different process than the light-toned layers on the plateau.

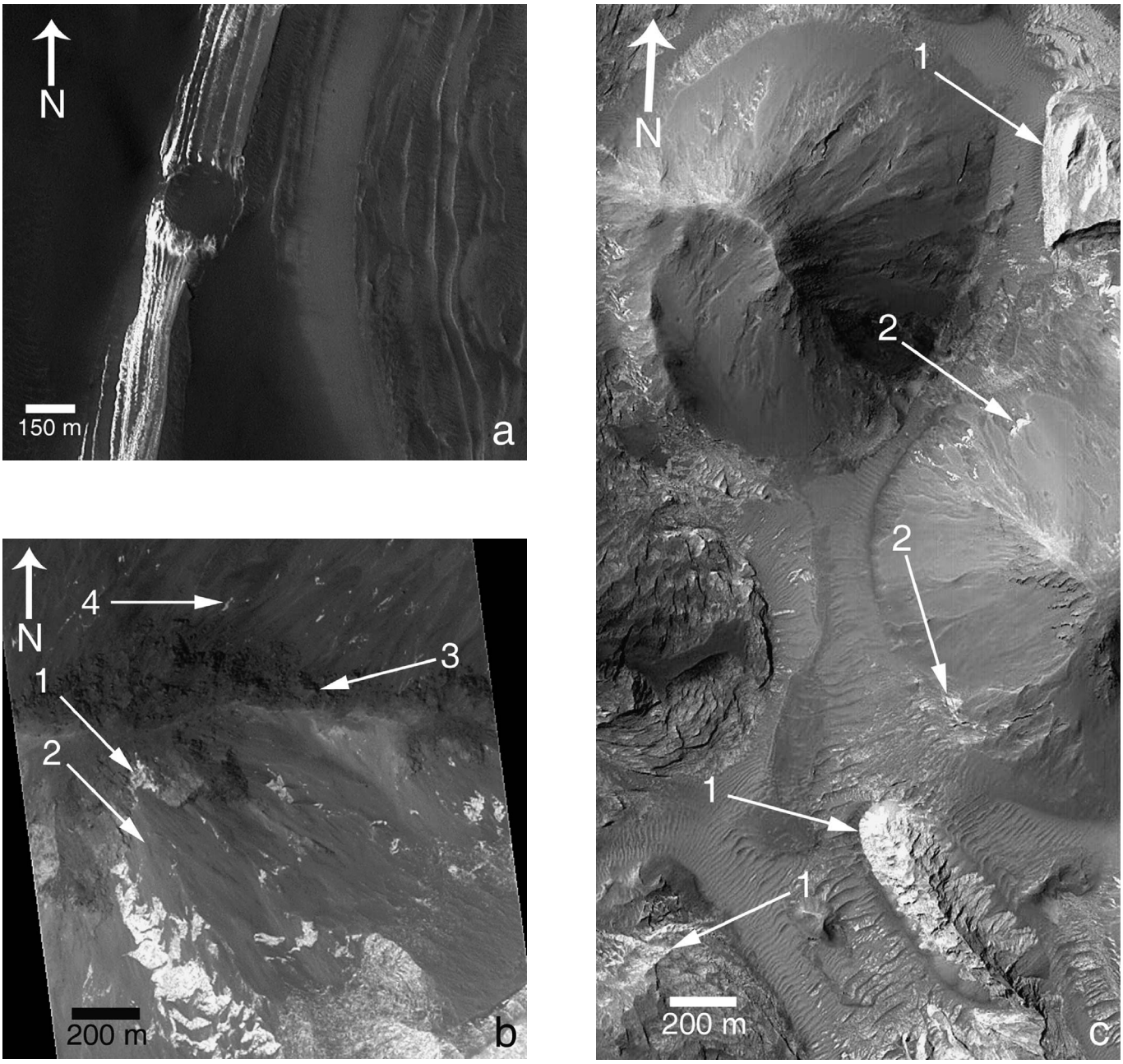

Fig. 9. Examples of outliers of LLO material. (a) Portion of M0303131 showing buried layered LLO material near the west edge of 'C.' Note the 150-m-diameter impact crater. (b) Portion of M1000466 showing patches of LLO material at a rocky ridge projecting from the chasm wall just north of LLO 'A.' Light-toned material (arrow 1) has been exposed just below the ridge crest by a recent talus slide (arrow 2). On the north side of the ridge capped by apparent wall rock (arrow 3) small exposures of light-toned material can be seen in an area of active mass wasting (arrow 4). (c) Portion of E2200455 in chaotic terrain east of 'D.' Blocks and mounds of LLO material (arrows 1) are exposed between mounds and dark plateaus of chaotic terrain. Note the apparent exposures of LLO material on the lower slopes of a chaotic terrain mound (arrows 2).

4.2. Morphology of the major outcrops of light-toned layered material

The major LLOs in Juventae Chasma exhibit a variety of surface morphologies (Table 2): fine layer structure down to 10-m scale (Fig. 11), cuspate sculpted ridges often resembling yardangs (Fig. 12a), bench and cliff structure at 100-m horizontal scale sometimes occurring with superimposed decameter scale roughness (Fig. 12b), and cliffs that are usually associated with intermediate-toned debris aprons, often concentrated beneath alcoves (Fig. 12a). Sculpted ridges vary between LLOs, however, with the most flat-lying LLO ('D') exhibiting scattered cuspate ridges on a relatively smooth surface; 'A' and 'C' exhibit continuous sharply sculpted ridges on surfaces that are very rough at a scale of a few hundred meters, and 'B' exhibits an intermediate style with smoother but fairly continuous apparent yardangs. Prominent alcoved cliffs with intermediate-toned debris aprons bound parts of 'A' (Fig. 12a) and 'C' (see

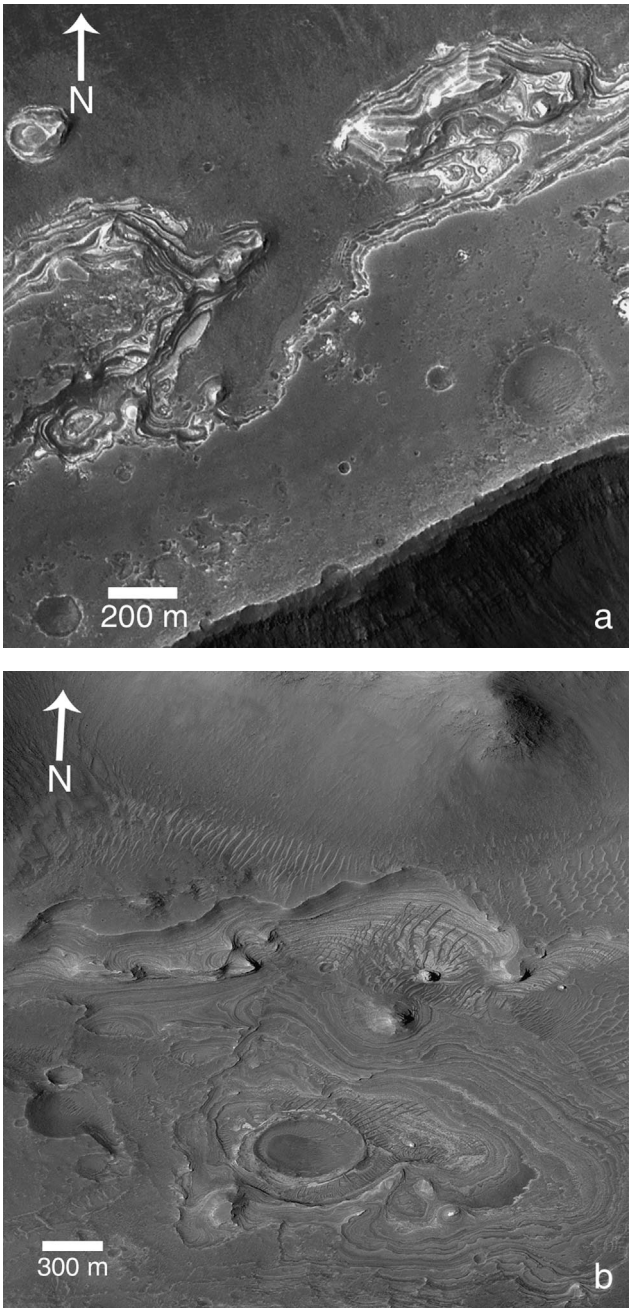

Fig. 10. Exposures of apparent LLO material on the plateau west of 'A.' (a) Portion of R0400556 showing light-toned layered material exposures near the edge of Juventae Chasma. (b) Portion of R0401800 showing exposures of light-toned layered material in a depression on the plateau west of 'A.' (c) MOC wide-angle context image (R0401801) showing the locations of (a) and (b).

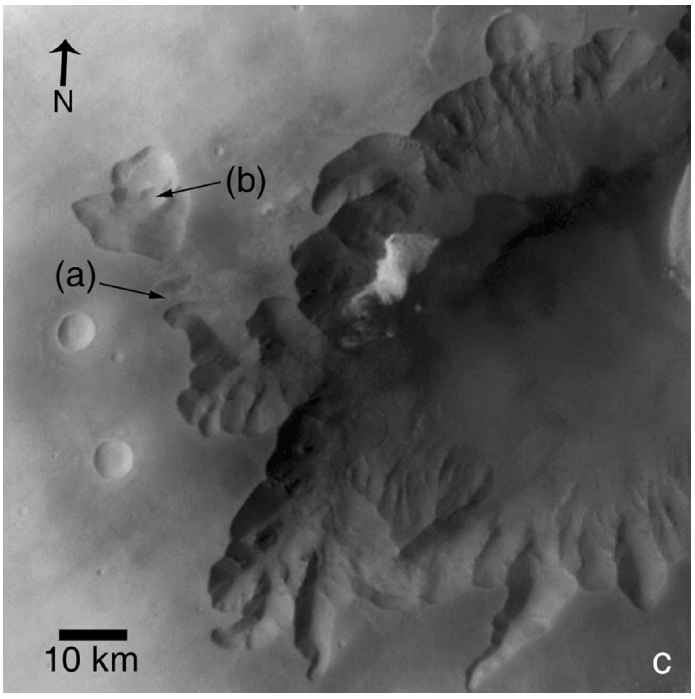

Fig. 10. (*continued*)

E1200829). A small cliff with debris aprons also occurs along part of the north edge of 'D' (E2200892). No bounding alcoved cliffs have been identified on LLO 'B' but intermediate toned debris is found on cliffs in a bench and cliff structure (Fig. 12b).

4.3. Thermal inertia of the LLOs

All of the LLOs exhibit light-toned surfaces that are brighter than nearby dust, sand, or rock, though dark sand and/or intermediate-toned dust forms patches on the LLOs. Fig. 13 shows THEMIS-derived thermal inertia maps for LLOs 'A,' 'B,' and 'C.' Sufficient MOC NA images allow us to construct mosaics in Fig. 14 for LLOs 'A' and 'B' to be compared with Fig. 13. The thermal inertia values on the LLOs range from that for coarse sand, $\sim$400 $\mathrm{J\,m^{-2}\,s^{-1/2}\,K^{-1}}$, to as high as 850 $\mathrm{J\,m^{-2}\,s^{-1/2}\,K^{-1}}$. Where the thermal inertia is low, typically the corresponding derived albedo is low. The thermal inertia map also correlates well with the visual images. The best relationship between thermal inertia and albedo is for LLO 'A,' the brightest LLO (Fig. 15) suggesting that clean, bright surfaces are rocky. For LLO 'A,' thermal inertia clearly delineates the contact of the sand sheet with the hummocky terrain to its west and also clearly defines the border of the LLO itself (Figs. 13A, 14a). The relatively darker, northwestern part of LLO 'A' is partly covered with coarse-grained sand on the basis of its thermal inertia. For LLOs 'B' and 'C' the highest thermal inertias tend to be found in the brighter edge regions, particularly near the western edge. The generally high values of thermal inertia and the tendency for inferred albedo and thermal inertia to correlate strongly support the hypothesis that the LLO units consist of sedimentary rock covered with a variably thick layer of sand or dust (Table 1). For comparison, we calculated the THEMIS-derived thermal inertia for "White Rock" in Pollack Crater (8° S, 335° W), and obtained a value of $\sim$230 $\mathrm{J\,m^{-2}\,s^{-1/2}\,K^{-1}}$, consistent with the TES-derived value of 232 ± 14 $\mathrm{J\,m^{-2}\,s^{-1/2}\,K^{-1}}$ obtained by Ruff et al. (2001). The significantly lower thermal inertia values of White Rock compared to those for Juventae LLOs show that its upper surface is composed of a different material, most likely indurated dust as suggested by Ruff et al. (2001).

Table 2
Characteristic features seen in MOC high-resolution images of the four major LLOs in Juventae Chasma

	LLO 'A'	LLO 'B'	LLO 'C'	LLO 'D'
Fine layer structure	M0301709 M1000466 E1102581 R0200160	E2301035 E0202546	E2001880 M2301235 M1201070 M1102064 M0400651 M2100460 M0702818	E2201273 E1600591 E1401770 E2200892 E2200455 R1003583
Bench and cliff structure	None observed	M0701527 E1000940 E0202546 E2301035 E1101370 M1001391	M2301235 (?) M1102064 (?) M0400651 (?) M0702818 (?)	E1401770 (?)
Decameter scale roughness on benches and cliffs	None observed	M0701527 E1000940 E0202546 E2301035	None observed	None observed
Bounding alcoved cliffs and debris aprons	M1000466 E1102581	None observed	M0303131 E1200829 E2001880 E2001880 M2301235 M0702818	E1600591 E2200892
Cuspate sculpted ridges	M100046 E1102581	E2301035 M1000391 E1101370 E0202546	E1200829 E2001880 M2301235 M1102064 M1102064 M0400651 M2100460 M0702818	E2201273 E1600591 E1600591 E1401770 E2200892 E2200455 R1003583
Dark-toned capping layers	None observed	None observed	M2301235 M1201070 M1102064 M0400651 M2100460 M0702818	E2200455
Evidence for exhumation from walls or chaotic terrain	R0300948 M1000466 E1102581 R0200160	E0202546 E2301035 E1101370	M1102064 M0400651 M2100460 M0702818	E2201273 E1600591 E1600591 E1401770 E2200892 E2200455 R1003583 R1502329

MOC images are listed through mission phase R15. Question marks indicate uncertain identification.

4.4. Dark capping layers

On LLOs 'C' and 'D,' material covering part of the surface forms thick dark plateaus or capping layers associated with dunes (Fig. 16; see also MOC NA image M1201070). These dunes stretch downwind (southward) from the apparent source material. The capping layers often have light-toned edges and show underlying LLO material and so may consist of LLO material mixed with dark fines, which is released and blown downwind as the capping layers undergo wind erosion. Consequently, sometimes the dunes appear darker than our inferred source. A few small craters occur on the capping layers, but craters are almost entirely absent elsewhere on these major LLOs. The interpretation of the dark flat surfaces as capping layers, follows from their occurrence on the raised topography of an LLO unit, their bordering by light-toned exposures, the steep edges of the flat plateau surfaces, and typical LLO morphologies that extend beneath them. Chapman et al. (2003) also described a portion of the dark plateau on LLO 'C.' Where light-toned material is exposed, thermal inertia is relatively high (400–800 $J\,m^{-2}\,K^{-1}\,s^{-1/2}$). This thermal inertia is higher than that of the more flat-lying capping layers (280–320 $J\,m^{-2}\,K^{-1}\,s^{-1/2}$) and consistent with consolidated material covered with a variable but thin layer of sand and/or dust. Erosionally resistant capping layers have also been described in chaotic terrain elsewhere, such as Aram Chaos where they cap hematite-rich layers (Catling and Moore, 2003), and on other flat-topped mesas in Valles Marineris (Lucchitta et al., 1994).

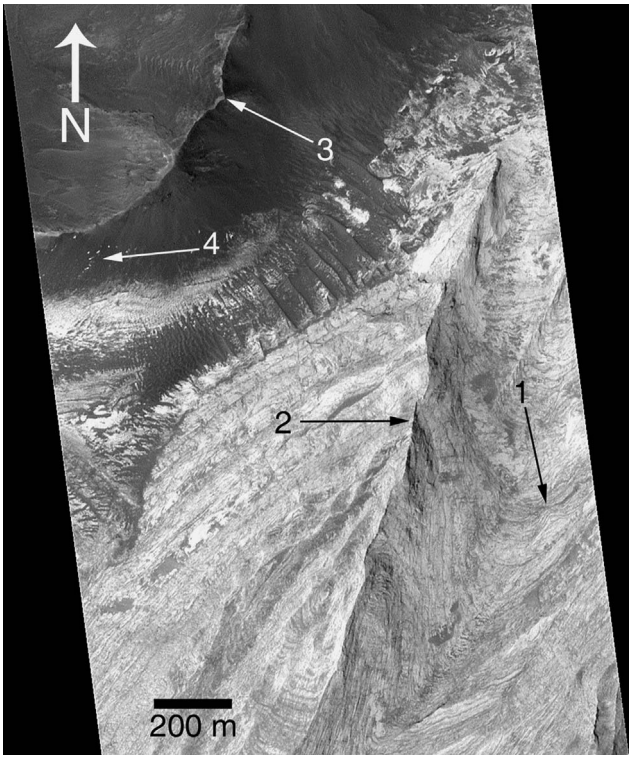

Fig. 11. Portion of MOC M1102064 showing fine layer structure (arrow 1) and cuspate sculpted ridges (arrow 2) near the northern edge of 'C.' Note the rocky ridge of chaotic terrain (arrow 3) with dark debris slides and some patches of exposed LLO material (arrow 4).

4.5. Evidence for exhumation of light-toned layered material

An issue of controversy has been whether LLO material outcrops from stratigraphic units that extend into the walls of Valles Marineris and associated chasms or whether LLOs are unconformably superposed on preexisting chasm topography. Malin and Edgett (2001) have promoted the former view, while other authors have generally argued for the latter (Lucchitta,

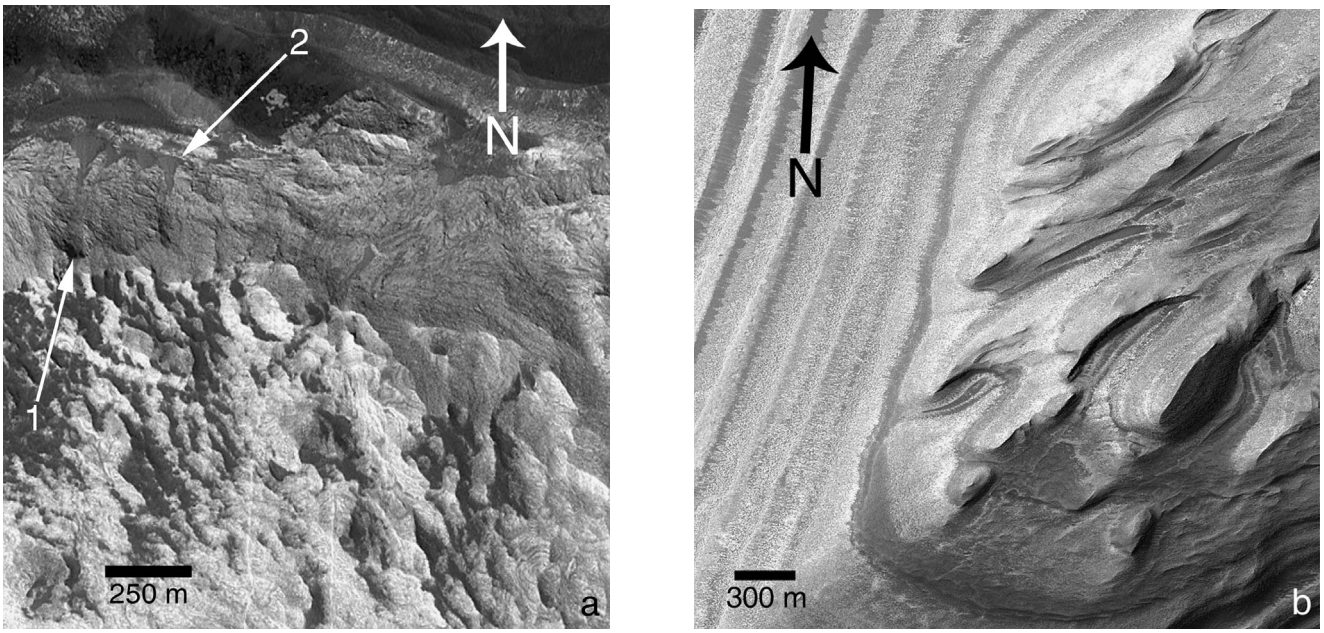

Fig. 12. Examples of cuspate sculpted ridges. (a) Portion of MOC E1102581 showing the north end of 'A.' Note the alcoved cliff (arrow 1) with some debris aprons (arrow 2) and the cuspate upper surface partially covered by dark sand or dust. (b) Portion of MOC E2301035 showing part of the top surface of 'B.' Note the cuspate ridges (right) above the bench and cliff structure (left).

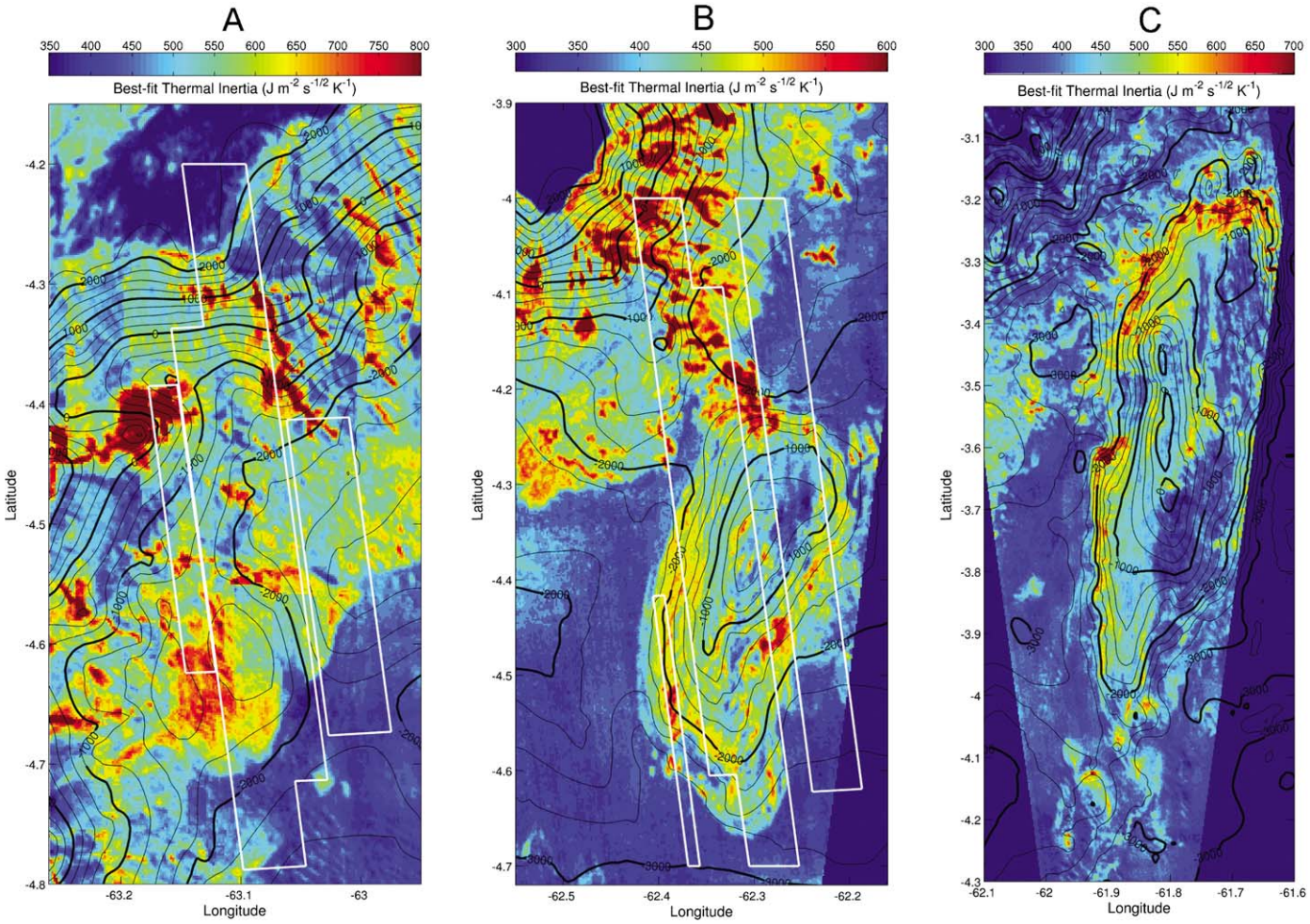

Fig. 13. Maps of derived thermal inertia for Juventae Chasma LLO's: 'A,' 'B,' and 'C.' Contours of MOLA topography data are shown at 250-m intervals (black lines). Also shown are the outlines (in white) of the images used for the MOC NA image mosaics of Figs. 14a and 14b.

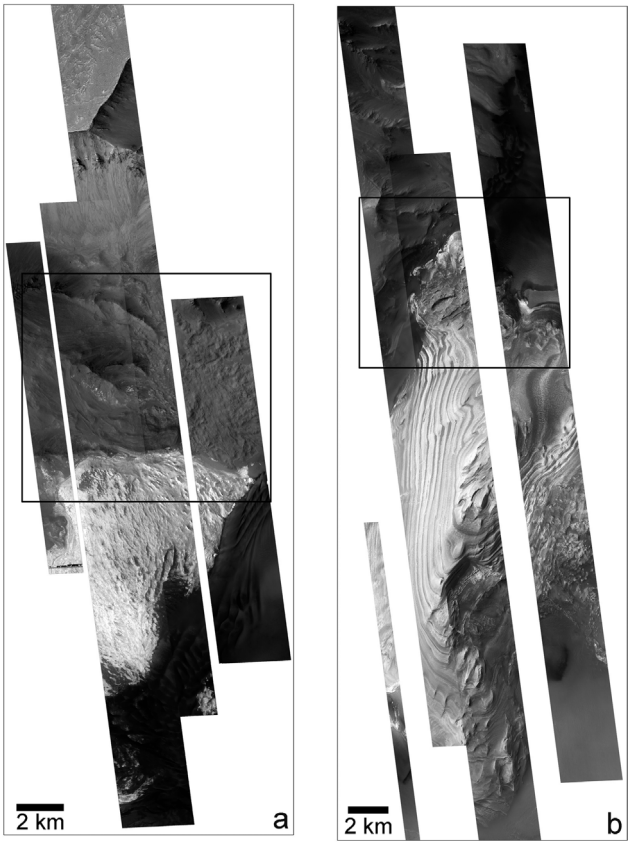

Fig. 14. MOC narrow angle image mosaics of (a) LLO 'A,' showing the inset for Fig. 19a; (b) LLO 'B,' showing the inset for Fig. 19b.

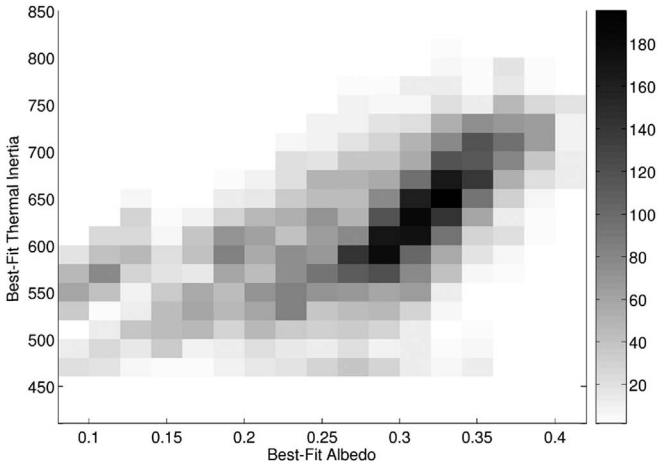

Fig. 15. Plot of derived thermal inertia vs derived albedo for LLO 'A,' showing a strong correlation between increasing albedo and increasing thermal inertia.

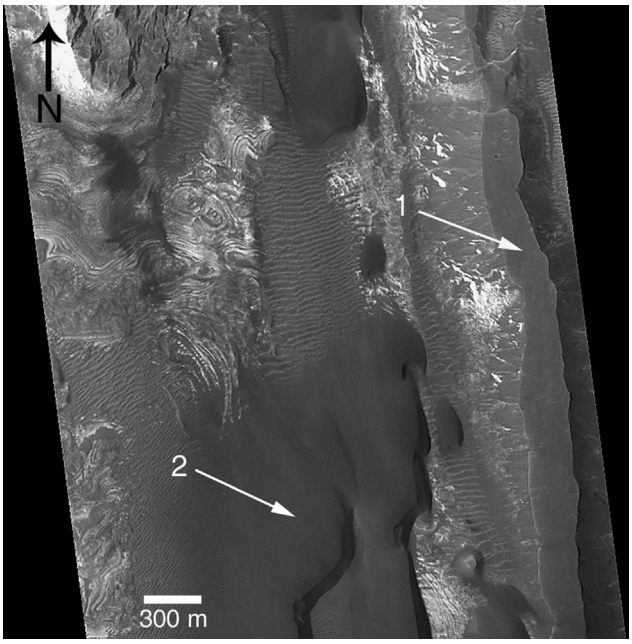

Fig. 16. Portion of M0400651 showing a dark capping layer in the form of a long narrow flat-topped plateau (arrow 1). Dark dunes (arrow 2) appear to be derived from similar capping layer plateaus farther north. Many small craters are visible on the plateau.

2001). For Juventae Chasma, in particular, previous authors have concluded that LLO material unconformably overlies the base of Juventae Chasma and adjacent lower portions of wall rock (Komatsu et al., 1993, 2004; Chapman and Tanaka, 2001). The idea that layered deposits formed within preexisting topography of Valles Marineris and associated chasms dates from the interpretation of relatively low-resolution Mariner and Viking images. The large number of high-resolution MOC images analyzed here reveals new details of the major LLOs plus numerous outliers of apparent LLO material that support the case for exhumation of LLO material from wall rock, chaotic terrain, the hummocky terrain unit, and the upper surface of the adjacent plateau above Juventae Chasma.

A clear stratigraphic relationship bearing on the issue of exhumation is that between LLO material and chaotic terrain. Fig. 17 shows a dark mound of chaotic terrain superimposed on the surface of LLO 'D' and nearby an adjacent mound with dark material covering the north side but removed to show underlying LLO material on the south side (arrow 3 in Fig. 17). Figs. 18a and 18b show other examples of rock-ridged chaotic terrain mounds that superpose the surface of LLO 'D.' In Fig. 18a, dark material covering the top of a conical mound has been eroded away for a substantial distance up the cone's slopes and a possible landslide has exposed LLO material within the cone.

It is interesting to note that whereas the chaotic terrain material is cratered, the LLO material is crater-free. Hence, once exhumed LLO material erodes relatively rapidly. One can infer that, over time, such LLO erosion would lead to degradation and lowering of superposed chaotic terrain mounds, even in the present epoch. Chapman et al. (2003) also identified LLO material "superposed by chaotic blocks" in M0804669. At the same time, Chapman et al. (2003) were puzzled by an apparent opposite stratigraphy at LLO 'C,' whose north end appears to superpose chaos based on a 72.5 m pixel^{-1} Viking Orbiter image, V0906A06. Examined with MOC images, the actual stratigraphy of the north end of LLO 'C' is more intricate. LLO material lies topographically below rocky ridges of chaotic terrain and emerges from dark material associated with the chaotic terrain (Fig. 11). The outliers shown in Fig. 9c are also closely associated with rugged ridges and mounds of

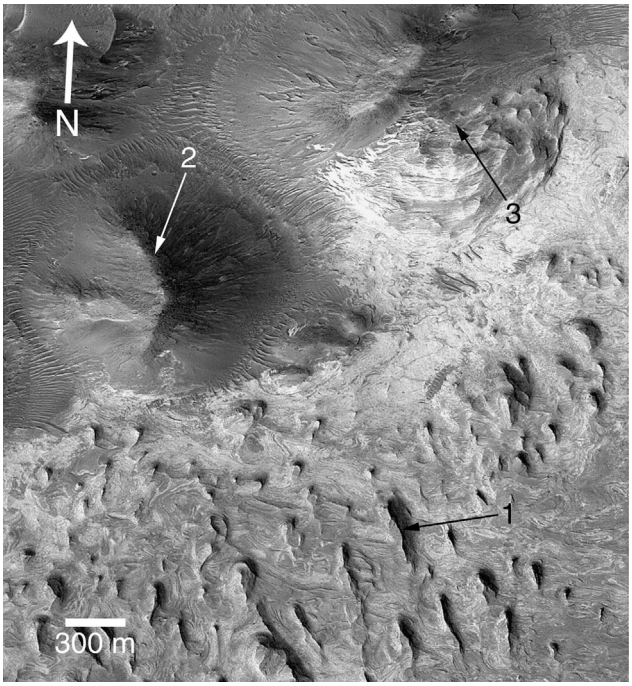

Fig. 17. Portion of R1003853 showing part of the north end of 'D' with one of the many cuspate ridges scattered across the surface (arrow 1), a dark chaotic terrain mound overlying LLO material (arrow 2), and a chaotic terrain mound with dark material covering the north (upper) side but with LLO material exposed on the south side (arrow 3).

chaotic terrain, and patches of light-toned layered outcrops can be seen on the slopes of these mounds. These outliers and another outlier cluster farther east (identified by Chapman et al. (2003) in M0804669) lie on opposite sides of a large patch of dark material that is the source of a long string of dark dunes. The extreme west end of the dark patch corresponds to a dark plateau (E2200455). This association between dark plateaus and dunes, similar to those seen on the surface of LLO 'C,' supports the inference that LLO material is emerging from beneath flat layers of chaotic terrain in this region (see also E1701902).

Evidence for exhumation of LLO material from beneath rocky ridges and spurs of wall material can be seen in Figs. 9b and 19a, just north of LLO 'A.' The dominant surface degradation process just north of 'A' is mass wasting, and several shallow landslides appear to have revealed underlying LLO material (arrows 1 and 2 in Fig. 9b). The other possibility is that these are remnants of an LLO that was unconformably deposited and subsequently eroded away to leave patches behind. However, if the LLO material were unconformably deposited and then eroded away then we should expect to see earlier stages of LLO against the chasm walls with positive relief, but we have not found such LLO material. The occurrence of LLO outliers on slopes on both sides of several rock-capped ridges north of LLO 'A' suggests to us that extensive deposits of LLO material lie beneath the dark, rocky material.

Evidence for ongoing exhumation of the north end of 'B' from beneath a spur ridge of wall rock can be seen in Fig. 19b and the associated composite elevation and thermal inertia map. This end of 'B' is a saddle along a major ridge extending down-

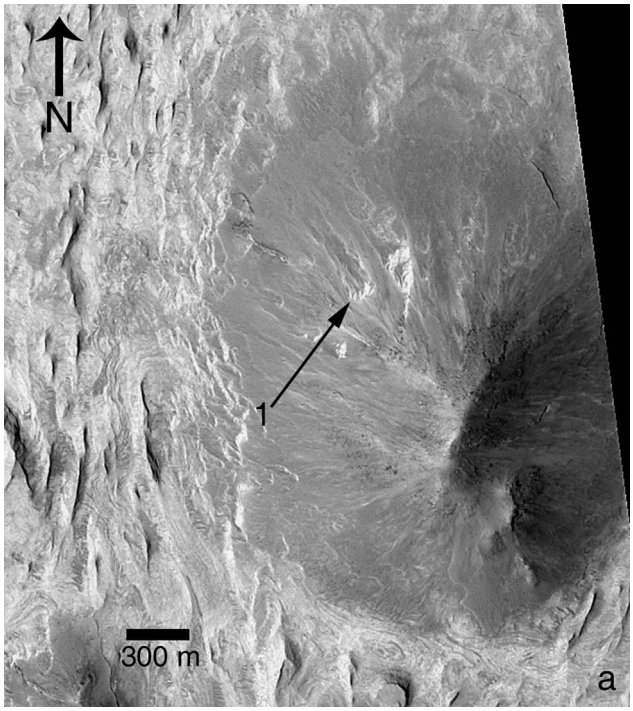

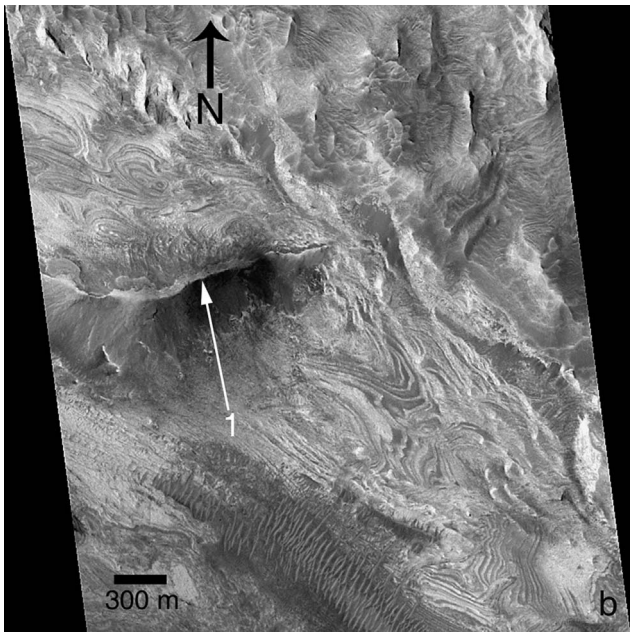

Fig. 18. (a) Portion of R1502329 showing an isolated chaotic terrain cone surrounded by the surface of LLO 'D' and clearly superposing it. Arrow 1 indicates LLO material exposed within a probable shallow landslide scar on the flank of the chaotic cone. (b) Another portion of R1502329 showing a chaotic terrain ridge superposed on the surface of LLO 'D' (arrow 1).

ward into Juventae Chasma from the plateau. The sculpted upper surfaces and a steep western slope exhibiting bench and cliff morphology extend under a narrow band of dark sand and scree at the base of a smaller scale curvilinear ridge that parallels the edge of the LLO. This ridge and a similar curvilinear ridge in light-toned material near the northeast corner of the LLO have high thermal inertia. The high thermal inertia area at the top of the LLO is separated from high thermal inertia dark rocky ma-

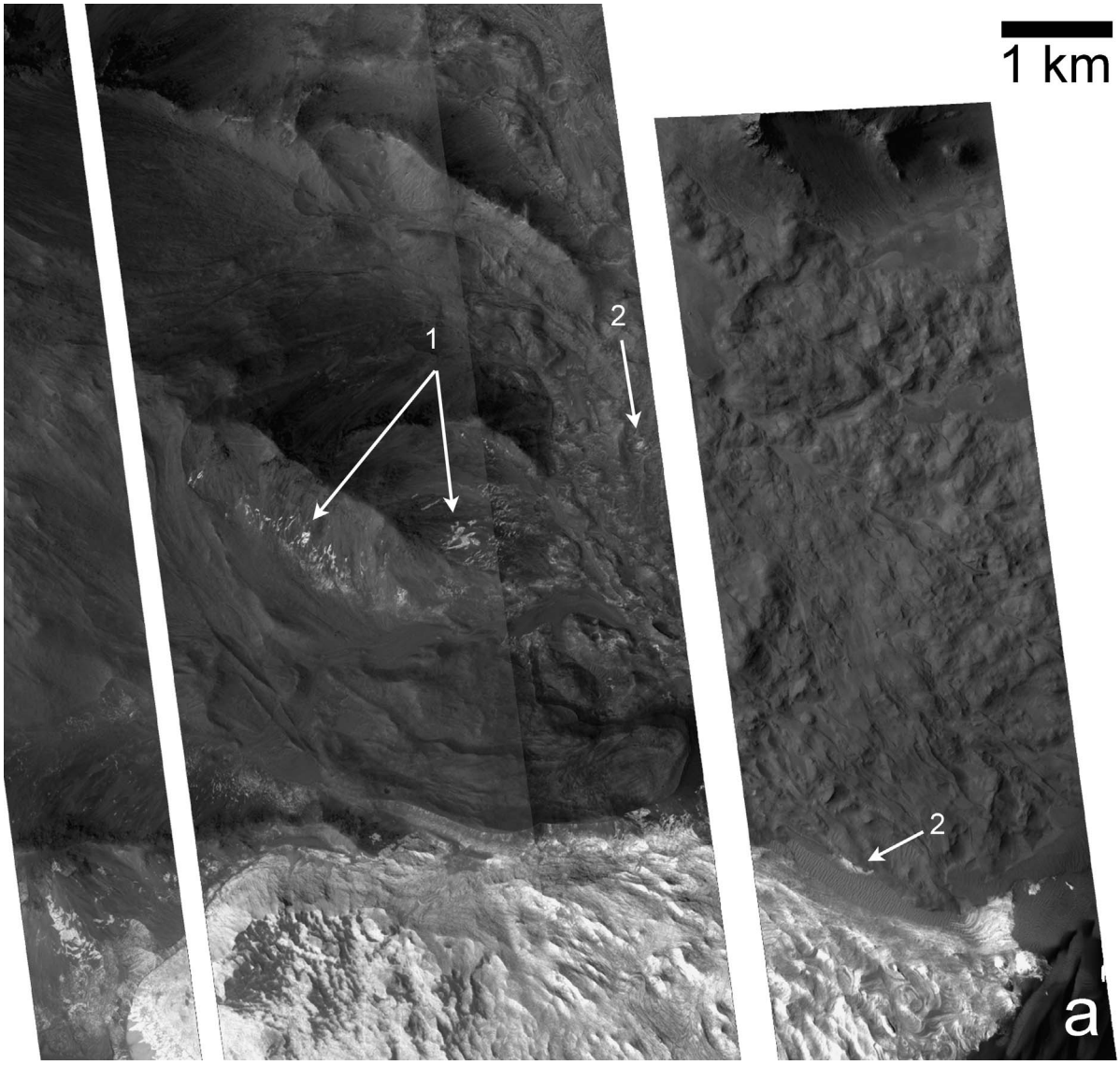

Fig. 19. (a) Detail from Fig. 14 of the of north end of 'A' showing ridges with exposures of light toned material on both sides (arrows 1) and hummocky terrain extending down from chasm wall. Light-toned material can also be seen within the hummocky terrain (arrows 2). (b) Detail from Fig. 14 of the north end of 'B' showing small patches of light toned material near the summit of a ridge of dark material (arrow 1) and morphologically similar curvilinear ridges in dark and light material (arrows 2).

terial of the ridge by a particularly narrow band of scree. Small patches of light-toned apparent LLO material can be seen just below the crest of the dark curvilinear ridge. Although these relationships do not prove exhumation, we think that this is the most likely explanation.

Further evidence for exhumation of LLO material is presented by light-toned layered material in the plateau depression west of 'A' (Fig. 10b, see also the overlapping high resolution MOC images R0500012 and R0501255). This eroding surface is unconformably overlain by a quasi-horizontal intermediate-toned surface that is overlain in turn by talus slopes of the walls of the depression. Partially exhumed LLO outcrops can also be seen within hummocky terrain near LLO 'A' (Figs. 5b, 19a). The hummocky terrain here appears to extend well up along the chasm wall. The texture of the hummocky terrain suggests the terrain could be landslides of material derived from the chasm wall or could be LLO material that is blanketed by darker toned cover or a combination of both.

Finally, we note that the emergence of other LLO material from beneath rocky ridges is observed elsewhere in the Valles Marineris system of canyons and chasms. A good example is shown in Fig. 20 in central Candor Chasma. Here layers on the northeastern side of a dark rocky ridge re-emerge and continue on the ridge's northwest side (arrow). This suggests that the dark, rocky material overlies the LLO material and that the LLO material is weathering out from beneath the ridge that superposes it. Given that the Candor Chasma LLOs are similar in albedo and morphology to the LLOs in Juventae Chasma and also contain a spectral signature of sulfate (Gendrin et al., 2005), it is not unreasonable to propose that both sets of LLOs may have formed by a common process that operated early in martian history.

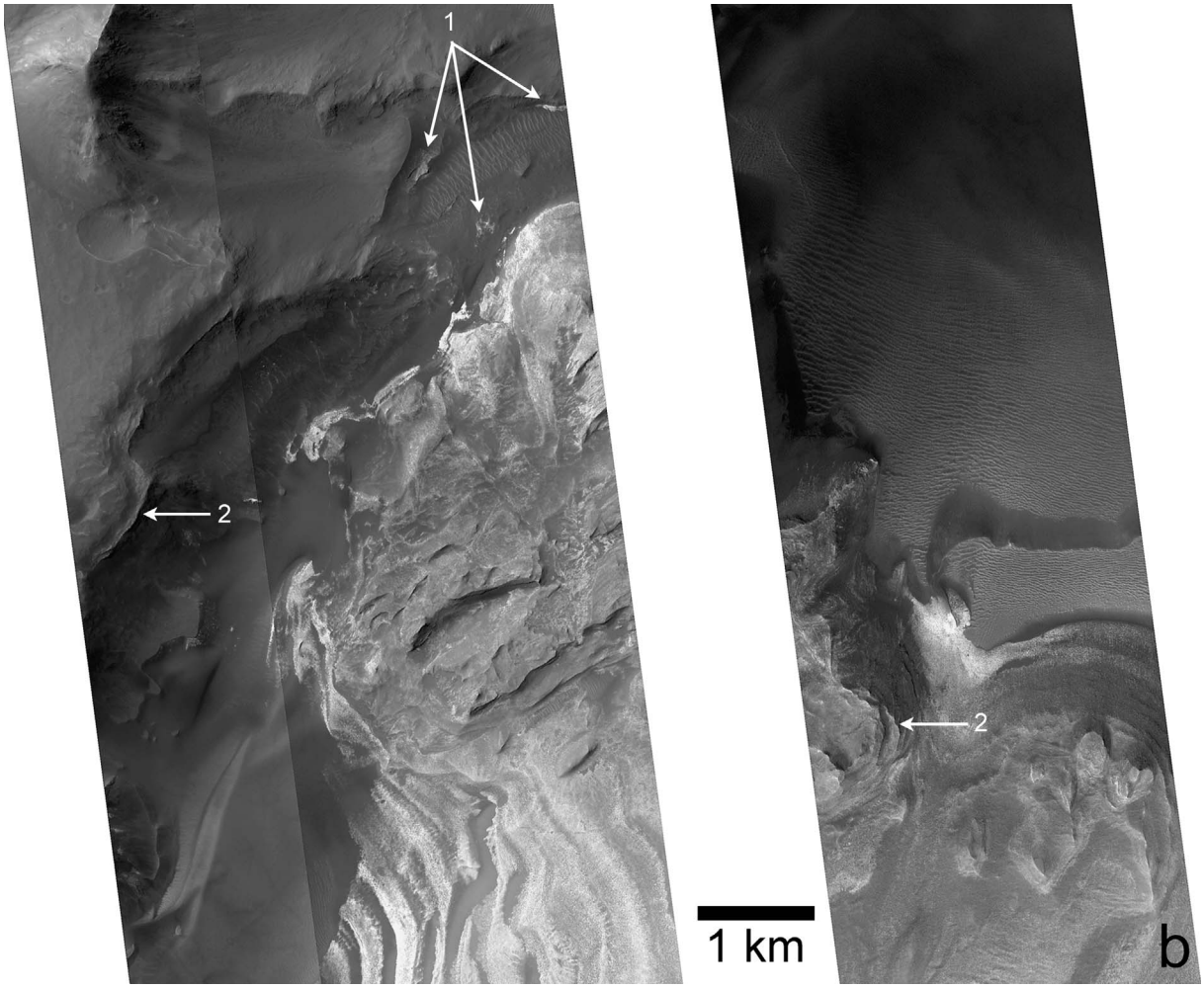

Fig. 19. (*continued*)

4.5.1. Erosional processes

Wind erosion and mass wasting are active processes in Juventae Chasma in the current epoch. The cuspate sculpting of the upper LLO surfaces and the almost complete absence of craters strongly suggests that wind erosion is the dominant process that deflates the LLO surfaces. On LLO 'A,' for example, the absence of small craters can be used to infer an approximate lower limit on the erosion rate, as follows. The rate at which craters should appear as a function of time and (image) area on Mars can be estimated from the cratering production function for Mars. The role of secondary craters may cause an error in estimating the rates (McEwen, 2004), but absence of small craters must still imply a lower bound on resurfacing. Using the method applied to the polar terrain by Herkenhoff and Plaut (2000), the production rate of craters with diameter >20 m is 5.6×10^{-9} km^{-2} yr^{-1}. A typical MOC narrow angle image of ~60 km^2 area with not a single crater implies <0.017 craters km^{-2} (=1 crater/60 km^2). Following Herkenhoff and Plaut (2000), this gives a surface age <9 myr, when multiplied by 3 to take account of Poisson statistics (i.e., 3×0.017 craters km^{-2}/5.6×10^{-9} km^{-2} yr^{-1}), and yields a resurfacing rate of >1–2 myr^{-1}. We suggest that wind is the most likely resurfacing agent. Clearly, since the Hesperian, kilometers of LLO material could have been removed.

In addition to wind erosion, bounding cliffs with intermediate-toned debris aprons indicate that downslope gravitational movement of loose soil and rock particles, i.e., mass wasting, effectively erodes LLOs from the sides. Absence of large piles of obvious light-toned LLO material surrounding the major LLOs suggests that eroded LLO material mixes with sand and dust in the chasm and is gradually removed from the chasm by wind transport. The intermediate toned material may consist of a mixture of dark sand and light toned material or it may consist of a distinct intermediate toned material. In the latter case, the source of the intermediate-toned talus debris aprons may be from within the LLO material itself. Hydrous sulfates have been identified in the surface of LLO 'B' (Gendrin et al., 2005), so it is reasonable that the other major LLOs and outliers in Juventae Chasma probably consist of sulfate minerals in various hydration states. Sulfates on Mars are readily eroded by the wind, as observed at the Opportunity rover site (Squyres et al., 2004a), which supports our observations of LLO erosion in light of the identification of these materials as sulfate-bearing.

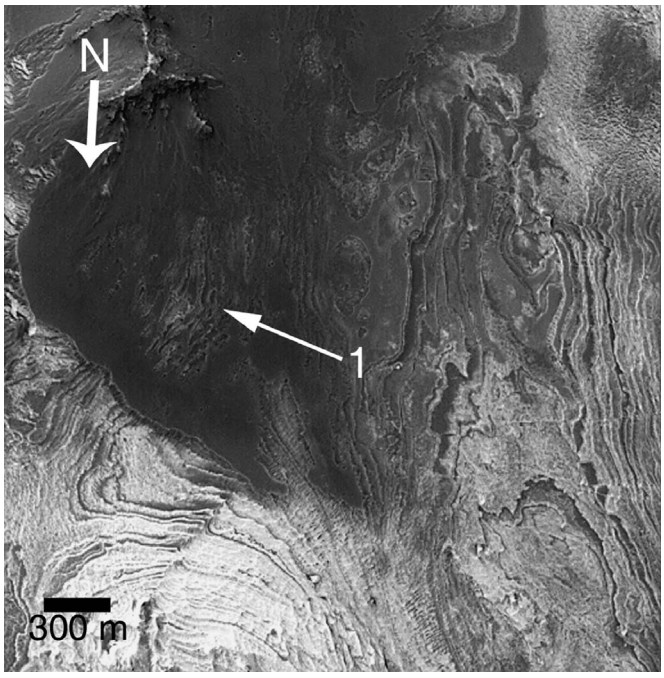

Fig. 20. Portion of MOC M1700467 in central Candor Chasma. Light-toned outcrops of layered material pass below a dark-toned ridge and emerges the other side of the ridge (arrow 1). This suggests that the layers are weathering out from underneath the ridge, which superposes it.

Differences in characteristic morphologies of the LLOs could be due to differences in sulfate hydration state, initial topography, formation processes, or exposure age. Given the association of sulfates with a hematite lag that forms when the sulfates erode through wind at the Mars rover sites (Squyres et al., 2004b; Herkenhoff et al., 2004), we speculate that intermediate toned aprons may be analogous lags, noting that the spatial scale of the aprons is too small for mineral identification with TES.

4.5.2. Inferences from layering

The large flat-bedded areal extent of fine layers are an important clue to the formation of LLOs. The fine layers in 'A' (Fig. 12a), and 'C' (Fig. 11) have a distinctly sedimentary character. In particular, as previously noted by Komatsu et al. (2004), 'B' displays 10-m scale cross-bedding (M1001391). LLO 'C' also displays possible 10-m scale cross-bedding (M1102064). Such sedimentary deposition would be consistent with aqueous or sub-aerial deposition, which we further discuss in Section 5.

The occurrences of dark capping layers on the surfaces of 'C' and 'D' and the association of similar dark plateaus with small outlying LLO mounds in chaotic terrain west of 'D' suggests that portions of 'C' and 'D' are emerging from beneath the dark capping layers as the process of formation of chaotic terrain proceeds even today. The superposition of mounds of chaotic terrain material on LLO 'D' supports this inference of continuing evolution of chaotic terrain. Derivation of chaotic terrain from collapsed wall rock would imply that the underlying LLO material must predate Hesperian lava flows that define the upper wall of Juventae Chasma.

5. Summary of results and inferences for the LLOs

Below we summarize our findings and then, in light of these findings, we discuss the implication for the origins of the LLOs in Section 6. We have determined the following:

(1) The thermal inertia of the LLOs ranges from ∼400 to 850 $\mathrm{J\,m^{-2}\,s^{-1/2}\,K^{-1}}$. The lower values are associated with darker regions that we interpret as partial sand-cover. The high values of thermal inertia are consistent with material that is much more consolidated than indurated dust. Given the detection of hydrous sulfates by Mars Express OMEGA on Juventae Chasma LLOs (Bibring et al., 2005; Gendrin et al., 2005), the LLOs apparently consist of consolidated salt deposits probably mixed with dust and sand.

(2) Light-toned layered outcrops observed in MOC images and measured by MOLA have a continuous elevation range in the chasm from −3.2 to +0.3 km (Fig. 8b). Light-toned layered material is also present within a depression to the west of Juventae Chasma at an elevation of ∼0.8 km, and on the plateau surrounding the chasm at an elevation of ∼2.6 km. Thus, the elevation maximum and minimum of the light-toned layered material are 2.6 and −3.2 km, respectively, which gives a total range of 5.8 km. The plateau surrounding the chasm is of Hesperian age. The basement of Juventae Chasma beneath the LLOs is older, probably consisting of Noachian lava flows. Consequently, light-toned layered material apparently formed over an exceedingly extensive period of time. Any hypothesis for the origin of the light-toned layered materials must explain their wide distribution of elevations and locations.

(3) The aforementioned observations (and the distribution of outliers in Fig. 8, in particular) suggest that the LLO material within Juventae Chasma was much more extensive than we see today. Indeed, the surfaces of the LLOs typically have very few, if any, craters at the decameter scale or larger. The absence of small craters implies that LLOs are actively eroding at a rate of order at least ∼1 $\mathrm{km\,byr^{-1}}$. Consequently, the LLOs must have been much more extensive in the past and it is conceivable that several kilometers depth of LLO material have been eroded away during the Amazonian.

(4) We find that the geomorphology and elevation range of the LLO material is most consistent with LLO material being exhumed from wall rock, chaotic terrain, and the hummocky terrain. This view is most compelling in images of LLO material weathering out from below and within rocky-surfaced chaotic terrain (Figs. 17 and 18). This leads to the important conclusion that deposition of the LLOs within Juventae Chasma predates the Hesperian plateau above the chasm.

(5) In certain places, we find relatively dark capping layers on LLO material. The presence of craters on the capping layers but not on the associated LLOs suggests that the capping layers are more resistant to wind erosion than the LLO material. On LLO 'C' especially, it appears that erosion of LLO material is causing capping layers to collapse from

the edges with the resulting loose talus sliding down slope, exposing more of the underlying LLO, and thereby feeding back to further capping layer collapse. Dark dunes likely form from material eroded from dark capping layers. We speculate that the capping layers may be indurated material (e.g., indurated ash) that was deposited on top or perhaps within the LLO material. The occurrence of capping layers and rocky chaotic mounds on top of LLO material leads to the important conclusion that chaotic terrain continues to evolve in Juventae Chasma even today.

(6) We identify the presence of possible fluvial strath terraces along Juventae Chasma's upper wall (Fig. 6). The elevation of these terraces, which is above the "pour point" of Juventae Chasma (Fig. 3), could have facilitated downslope fluid flow that formed Maja Vallis. The elevation of the fluvial straths indicates that channels started forming either before or contemporaneous with Juventae Chasma, at a time that would postdate the deposition of Juventae Chasma LLOs.

Considering all of the above, we can make some general inferences about the geologic history of Juventae Chasma. It is generally believed that the Valles Marineris canyon system formed from a combination of downfaulting along faults radial to the Tharsis bulge and from erosional processes as evident from the dissection of walls by gullies, branching side canyons, and landslides. In the case of Juventae Chasma, catastrophic release of water into Maja Vallis, would have widened the chasm through collapse and break-up of material. Displaced blocks, such as those seen in the southern part of the chasm and chaotic terrain in the northern part of the chasm, are consistent with this hypothesis. Findings (2)–(5), lead us to conclude that the LLO material was emplaced prior to the Hesperian lava flows that form the plateau above Juventae Chasma.

It is not obvious how the apparent fluvial event in Juventae Chasma is genetically related to the LLO material. One possibility is that dewatering of hydrated salts in LLO material provided a source of water for the formation of Juventae Chasma from collapse and fluid outflow (Montgomery and Gillespie, 2005). Certainly, subsequent to the formation of the chasm, the erosion rate of LLO material has greatly diminished the spatial extent of LLO material. Consistent with large erosional loss of LLO material are remnants (LLOs 'A' to 'D') with considerable elevation range. We hypothesize that continuous LLO erosion by wind and mass wasting has led to diffusion and lowering of chaotic terrain during the Amazonian. The chaotic terrain apparently consists of old wall-rock material that has been lowered and reworked, and continues to be lowered due to LLO removal, even in the present epoch. Our view that chaotic terrain in Juventae Chasma continues to evolve contrasts with a prevailing view that chaotic terrain was formed on Mars in the late Hesperian or early Amazonian due to catastrophic flooding and has evolved little since.

6. Discussion on the origin of light-toned layered material

The various possible origins of LLO material that have been proposed in the literature were mentioned in Section 1. We now know that LLO surfaces are at least partially, if not dominantly, composed of sulfates. Here, we note that OMEGA is unable to detect anhydrous sulfates, such as anhydrite, even if it is present on dust-free surfaces of the LLOs. We can view LLOs in light of Mars exploration rover findings of sulfate-rich light-toned layered material (Squyres et al., 2004a). Taking these factors into consideration, the origin of LLOs comes down to three possibilities: (1) volcanic deposits (Lucchitta et al., 1994; Chapman et al., 2003; Komatsu et al., 2004), (2) lacustrine/marine sedimentary deposits formed either within the chasm or prior to its development (McCauley, 1978; Nedell et al., 1987; Komatsu et al., 1993; Malin and Edgett, 2000b), or (3) aeolian sedimentary deposits (Peterson, 1981; Nedell et al., 1987; Malin and Edgett, 2000b). We now discuss each of these possibilities in turn, in light of our geological findings.

6.1. Volcanic?

Although a volcanic origin of LLOs has been popular, we think that this possibility can be eliminated. The geomorphology argues against it: a lack of lava flow fronts, the presence of cross-bedded sedimentary layers (Section 4.5), the presence of hundreds of layers of similar thickness, and the lack of caldera. Indeed, the high-resolution stereo camera (HRSC) on Mars Express has shown that the layering of LLO 'B' is horizontal (Bibring et al., 2005), favoring a sedimentary rather than volcanic origin. Regarding caldera, Chapman et al. (2003) suggested small circular features in hummocky terrain just west of 'A' were possible volcanic vents. (This patch of hummocky terrain is not mapped on Fig. 4 because it is too small but is visible in MOC M10-00466.) However, the circular features occur where light-toned material is partially emerging from beneath dark sand or dust. The resulting complex albedo pattern makes morphological interpretation difficult. The majority of circular features in hummocky terrain elsewhere are impact craters.

A more serious problem with the volcanic hypothesis is that it is inconsistent with the geochemistry of the LLOs. Gypsum ($CaSO_4{\cdot}2H_2O$) on LLO 'B' has been inferred from near infrared spectroscopy from the Mars Express OMEGA instrument (Gendrin et al., 2005). Abundant gypsum would not be expected in either basaltic flows or basaltic ashfall. Moreover, thermodynamics shows that gypsum is a mineral that forms only at low temperatures; at higher temperatures, anhydrite ($CaSO_4$) is the thermodynamically favored form of calcium sulfate. The transition between gypsum and anhydrite is represented by the dehydration reaction

$$CaSO_4{\cdot}2H_2O \Leftrightarrow CaSO_4(s) + 2H_2O(l). \quad (1)$$

In dilute fluids, gypsum is produced only if the temperature is less than ~60 °C. For brines, the transition temperature is even lower. Fig. 21 shows the calculated transition temperature as a function of water activity, based on thermodynamic data and methodology given in Appendix B. Fig. 21 shows that in brines saturated with NaCl (a water activity of ~0.75), gypsum forms only at temperatures below ~20 °C.

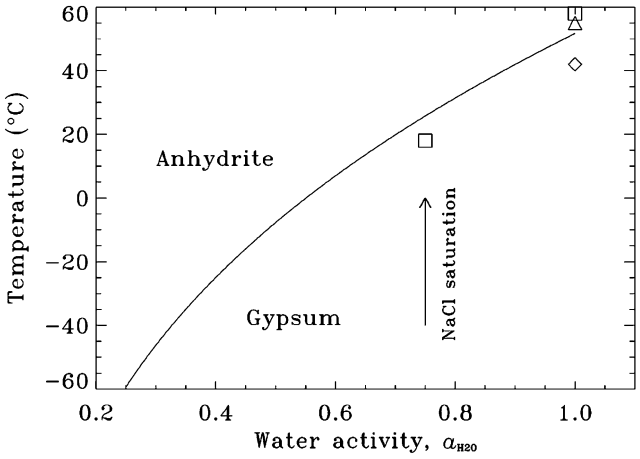

Fig. 21. The thermodynamic stability of gypsum compared to anhydrite. The transition boundary is calculated from thermodynamic data (see Appendix A). Squares (Hardie, 1967), the triangle (Knacke and Gans, 1977), and the diamond (D'Ans, 1968) indicate transition temperatures obtained in laboratory experiments.

6.2. Lacustrine/marine?

The most obvious connection of the LLOs to water is the presence of hydrated salts such as gypsum and kieserite. Mindful of the results from the Mars Exploration Rover Opportunity (Squyres et al., 2004b), one might hypothesize that the LLOs are large, sulfate-rich evaporite deposits comparable to Permian evaporites on Earth. Indeed, there are two possibilities for the formation of such evaporites in Juventae Chasma: either the evaporites formed in one or more bodies of water that filled that chasm after the chasm had opened or the evaporites formed from a body of water that existed before the chasm developed. There are problems with the former idea. First, we note that the summit of LLO 'C' at ∼257 m is quite close to the elevation of the chasm 'pour point' at ∼509 m (Fig. 3). Consequently, evaporites could not have precipitated from a single chasm-filling lake but could only have formed from repeated lacustrine episodes. Using MOLA data within Arcinfo, we calculate that the volume of water required to fill Juventae up to the pour point is 69,122 km^3. This volume is comparable to the volume of the largest inland salt lake on Earth, the Caspian Sea, which, at 78,200 km^3, contains about one third of Earth's inland water. Were evaporation of water in Juventae Chasma to have filled salt up to the top of LLO 'C,' the volume of salt would be 60,852 km^3. This is about 4% of volume of salt (1.6×10^6 km^3) estimated for the extraordinarily large Permian marine evaporites on Earth (Stevens, 1977). A sustained lake on Mars would have required an active hydrological cycle and sustained weathering and we might expect to see more signs of fluvial erosion than is evident. However, on Earth, when conditions have been favorable for deposition, very thick evaporites have been quickly produced: for example, a 1-km thick sequence of halite was deposited in the Miocene Mediterranean in less than 200,000 years (Schreiber, 1986). But the hypothesis of evaporation from a large chasm lake neither explains why we see light-toned layered material on the plateau above Juventae Chasma nor why LLOs are apparently being exhumed from underneath and within chaotic terrain.

The alternative idea that the LLOs derive from extremely ancient evaporites that formed prior to the development of Juventae Chasma can perhaps more easily be reconciled with the geomorphic evidence of exhumation of LLOs. It is also possible that catastrophic dewatering of preexisting hydrated sulfates was instrumental in the formation of the chasm, chaotic terrain, and Maja Vallis (Montgomery and Gillespie, 2005).

The presence of light-toned layered material on the sloping plateau above Juventae Chasma (Fig. 10a) is problematic for the idea that an evaporite origin is common to all LLO-like material. Certainly, the light-toned layered material on the plateau formed at a later time than the LLOs within the chasm. We leave open the possibility that the light-toned material on the plateau could be the result of an entirely different phenomenon from the chasm LLOs, though morphologically similar. For example, the plateau layers could be sub-aerially-deposited, salt-cemented dust from a much more recent era, whereas the LLOs down in the chasm could be sub-aqueous evaporites from early Mars. However, we note that the THEMIS-derived thermal inertia of light-toned material on the plateau is relatively high, around 500 J m^{-2} s$^{-1/2}$ K^{-1}, unlike "White Rock" in Pollack crater (Ruff et al., 2001).

6.3. Dry deposition in polar-like deposits?

A very different hypothesis for the formation of the sulfates is that they resulted from airfall. Here, there are two possibilities. Either sulfates accumulated as a result of purely dry deposition from the atmosphere or sulfates were concentrated by co-precipitation with icy materials, such as snow.

That sulfates can accumulate as a result of dry deposition is demonstrated on Earth from isotopic analysis of salts in the Atacama desert (Michalski et al., 2004). Atacama sulfate deposits have built up solely due to gradual dry deposition of sulfate that ultimately originates from gas to particle conversion of SO_2. Dry deposition of sulfate has long been expected on Mars (Settle, 1979) and is supported by isotopic geochemistry in the martian meteorites. Sulfur isotopes in meteorite sulfates are mass-independently fractionated, which is known to arise due to the interaction of ultraviolet radiation with atmospheric gases in certain photochemical processes. The fractionation pattern strongly suggests that sulfates were deposited by photochemical conversion of atmospheric SO_2 to sub-micrometer particles and subsequent dry deposition (Farquhar et al., 2000). It is well known that heterogeneous conversion of SO_2 to sulfate is much more efficient than purely gas phase reactions (Seinfeld and Pandis, 1998). Thus, a promising way to concentrate sulfates formed in the atmosphere is through co-precipitation with icy particles. A scenario we envision concerns snow or ice that accumulated in the tropics during repeated cycling of the orbital elements of Mars over geologic time. Periodic values of obliquity exceeding ∼45° are expected to cause ice on Mars to migrate from the poles to the equatorial regions (Haberle et al., 2003). Recent calculations suggest that the average obliquity for Mars over geologic time was ∼40° unlike 25.2° today,

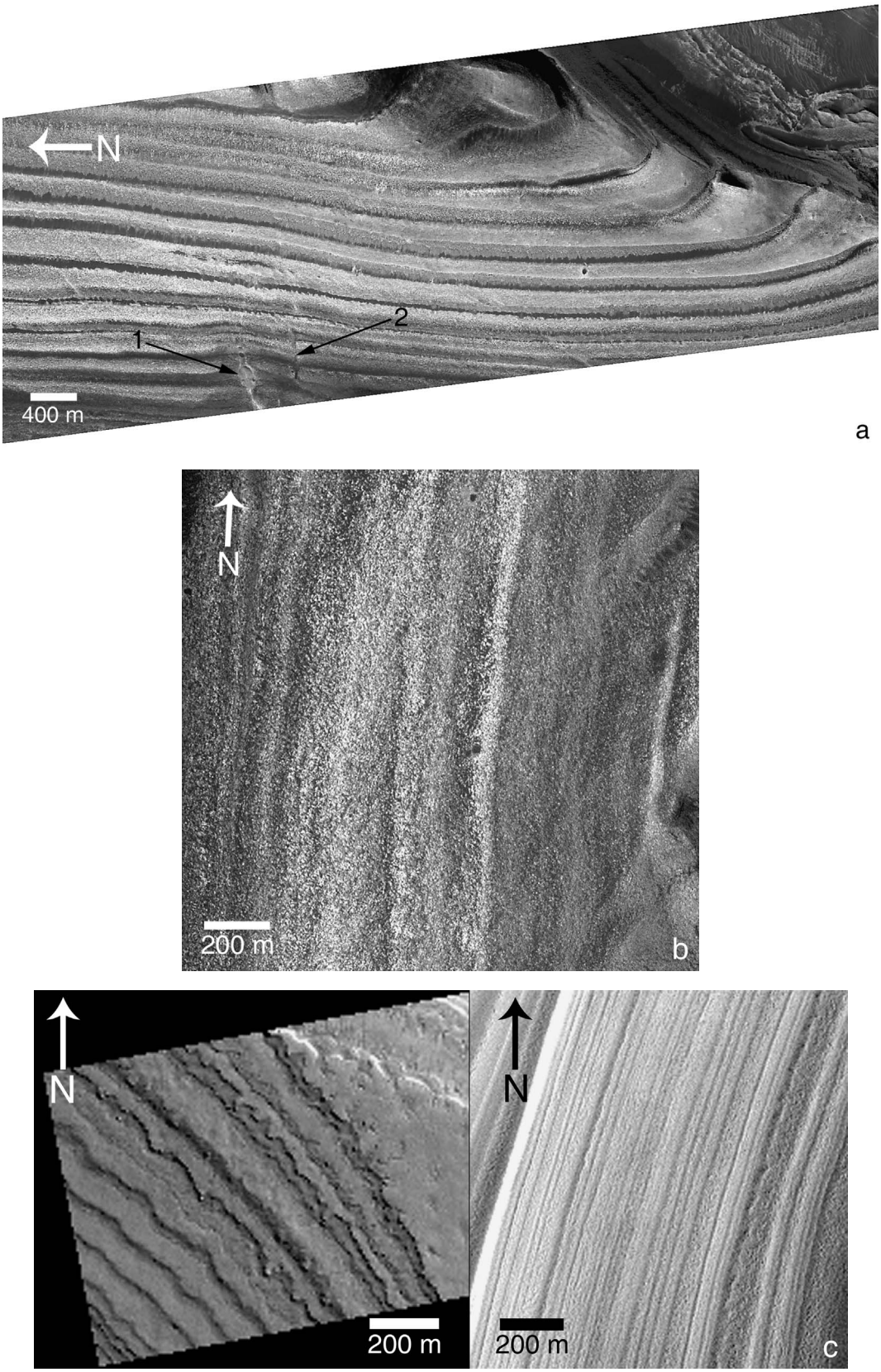

Fig. 22. Bench and cliff structure on 'B' and on the permanent south polar cap. (a) Portion of E0202546 showing decameter scale roughness superposed on bench-cliff structure and wrapping around a 'nose' of the LLO. Note the unusual features marked by arrows suggestive of gullies formed by very localized fluid runoff. (b) MOC M0701527 showing bench and cliff structure with superimposed decameter scale roughness in an image with 1.43 m pixel^{-1} resolution. (c) Left: An example of bench and cliff structure with decameter scale roughness on the permanent south polar cap (portion of M1300253). Right: Portion of E1800831 (near 82° N) showing decameter-scale roughness on the permanent north polar cap in an image with 5 m pixel^{-1} resolution.

and that sometimes the obliquity may have reached as high as ∼80° (Laskar et al., 2004). Consequently, extended periods of high obliquity may have been common before and during the early stages of Tharsis emplacement (Armstrong et al., 2004). For a considerable fraction of early martian history, the tropics would have been subject to accumulation of icy particles, even if the martian atmosphere and climate were little different from today. However, volcanism was certainly more active on early Mars as evidenced by lava flows, and the geochemistry of Mars inferred from martian meteorites suggests that the martian volcanic volatiles would be unusually rich in sulfur compared to terrestrial volcanic gases. Significantly, Wänke and Dreibus (1994) argue that martian volcanism would produce sulfur gases in greater abundance than water vapor, in stark contrast to terrestrial volcanoes. Thus, snow on early Mars may have incorporated unusual quantities of sulfate aerosol. In periods of low obliquity, ice is unstable in the martian tropics and would sublimate away (Mellon and Jakosky, 1995; Haberle et al., 2003), leaving rhythmic layers of hydrous sulfate mixed with dust, resembling present-day polar caps on Mars. A common process could thus explain the occurrence of light-toned layered material both in the depths of Juventae Chasma and the top of the plateau.

There are also morphological similarities of the LLOs to polar terrain, although we note that this does not necessarily indicate common process. LLO 'B' uniquely displays well-defined 100-m scale bench and cliff morphology shown in Figs. 12b and 22. This morphology bears some resemblance to characteristics seen in both polar caps (Malin and Edgett, 2000a). On the one hand, the bench and cliff topography is reminiscent of the surface of the permanent south polar cap, while the albedo variations are similar to those seen in the ridge-trough terrain of the permanent north polar cap. Also, a decameter scale roughness (Fig. 22b) resembles roughness at the same scale on the surface of the north polar cap (Fig. 22c). Some unusual channels that cut through the bench cliff topography are perhaps suggestive of gullies formed by small fluid runoffs (Fig. 22a). Possible remnants of bench and cliff morphology can also be seen on LLOs 'C' and 'D,' but the structure is highly degraded and there is no clear evidence for decameter scale roughness like that found on 'B' in Fig. 22b.

Given the long time for deposition, a polar-like airfall hypothesis would be consistent with apparent interleaving of LLO material with dark erosionally resistant material that has formed capping layers and that perhaps could be possible indurated ash layers. If hydrous sulfate layers were buried to depth or subject to geothermal heating at shallower depth, it is thermodynamically inevitable that the salts would dewater (Montgomery and Gillespie, 2005). Thus, we are mindful that liquid water would almost certainly have reworked sulfate deposits even if they originated from airfall and polar-like terrain.

7. Conclusions

We interpret the light-toned layered deposits in Juventae Chasma as sulfate-rich sedimentary rocks on the basis of geomorphology, geochemistry and thermal inertia, and we dismiss the possibility that they are volcanic deposits. Two origins remain plausible within the limited constraints of the orbital data. The light-toned material may have formed as an evaporite from a large sea that existed in the Noachian or early Hesperian prior to the development of Juventae Chasma. Alternatively, the light-toned deposits were built up by dry deposition of volcanic sulfate aerosols, most likely in association with the deposition of low latitude snow/ice containing sulfate-rich aerosols during ancient obliquity cycles. Sublimation and/or melting of ice and subsequent diagenetic re-working of the sulfates may obscure their exact origin when viewed from a purely geomorphic perspective, although they could be geochemically distinctive.

Acknowledgments

This research was made possible with NASA Mars Data Analysis Program (MDAP) Grant NNG04GK42G. We thank Steve Ruff and Cathy Weitz for detailed reviews.

Appendix A. Derivation of thermal inertia from THEMIS infrared data

A.1. Motivation and method

Thermal inertia (TI) is an important measure of the physical character of the surface at micrometer–centimeter depth scales. TI is the material property which controls the rate of heat flux into the subsurface, and is equal to $(k\rho c)^{1/2}$, where k is the thermal conductivity, ρ is the bulk density, and c is the heat capacity. For a given periodic surface heating rate, TI is the most important parameter in determining the amplitude of the resulting surface temperature variation (Carslaw, 1959; Kieffer et al., 1977). The primary source of variability in the TI of martian surface materials is the thermal conductivity. The quantity ρc varies by only a factor of 5 for most geologic materials, whereas k can vary by a factor of 1000 due to variations in particle size, air pressure (in the pore spaces), and the nature and degree of intergranular bonding or cementation.

Previously, TI has been derived from TES thermal infrared data using nighttime observations combined with independently measured surface albedo (Mellon et al., 2000; Putzig et al., 2005). While this technique is valid for the low TI values of most martian surface materials ($<250\ \mathrm{J\,m^{-2}\,s^{-1/2}\,K^{-1}}$), the nighttime temperature of higher TI materials becomes increasingly sensitive to the assumed value of the surface albedo. As shown in Fig. A.1, the slope and orientation of the surface also strongly affect the derived TI; but considering, for example, only nearly flat surfaces ($\theta < 5°$) in Juventae Chasma with an observed pre-dawn temperature of 200 K, derived TI values range from 350–550 $\mathrm{J\,m^{-2}\,s^{-1/2}\,K^{-1}}$ due to the variation in albedo values. Also the best available surface visible albedo measurements from the MGS TES, via a visible broadband channel of 0.3–2.7 μm (Christensen et al., 1992), have a spatial resolution of 3–6 km pixel^{-1}, which is far too coarse to resolve many features of interest in Juventae Chasma, such as the spatial details of LLOs. However, the resolution of THEMIS IR images (100 m pixel^{-1}) is sufficient for LLO analysis and slope

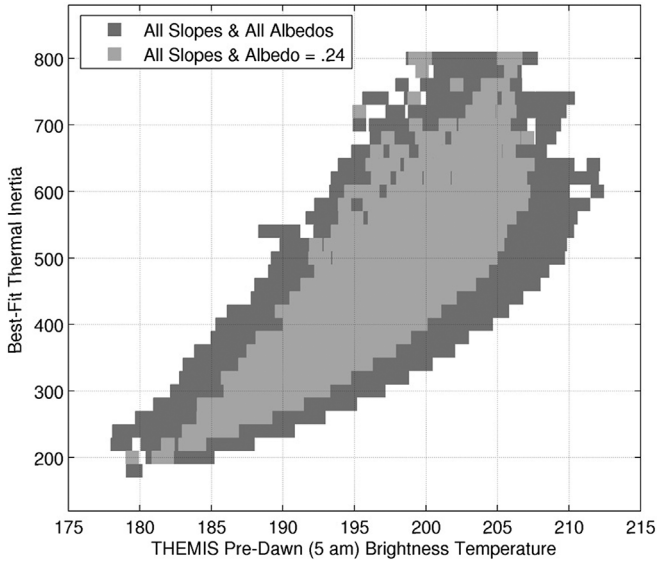

Fig. A.1. Range of variation in the best-fit thermal inertia values for sloped surfaces in Juventae Chasma plotted as a function of the observed pre-dawn brightness temperature. To isolate the effects of slope (0–48°) from albedo variations (0.1–0.4), we have highlighted the subset of pixels with a constant best-fit albedo equal to 0.24 using a lighter shade of gray.

effects can be accounted for by using MOLA data, as we now describe.

The slope and azimuthal orientation of the surface strongly affects surface temperatures throughout the day. We obtained values for the slope (θ) and azimuth (φ) angles of surfaces in our study regions from the 128 pixel degree^{-1} MOLA topography. The MOLA spatial resolution at equatorial latitudes is coarser than THEMIS data (∼400 m vs 100 m), so we first performed a bilinear interpolation of the MOLA elevation data down to the THEMIS resolution, before calculating slopes. We use slope angles in a one-dimensional thermal model (described below) to account for local effects such as the change in solar incidence angle and local horizon. Other three-dimensional effects such as shadowing or reflected and emitted radiation from other surface elements, which would require a much more complex topographic thermal model with ray-tracing algorithms.

We used a finite-difference, time-stepping model based on the Viking Thermal Model (Kieffer et al., 1977) which has been used in modified forms for many other studies of planetary surface energy balance, (e.g., Paige and Wood, 1992; Paige et al., 1994; Vasavada et al., 1999). The model calculates the surface temperature required to conserve radiative and conductive heat balance at the surface, and the one-dimensional thermal diffusion equation is solved numerically for each of 40 sub-surface layers of increasing thickness extending to several times the annual thermal skin depth. For this study, we assumed the thermophysical properties did not vary with depth, and the broadband thermal emissivity of the model surface was 0.95. Radiative heating of the surface by atmospheric thermal emission was parameterized as 2% of the local noontime insolation, following Haberle and Jakosky (1991); and turbulent heat exchange with the atmosphere was neglected.

The THEMIS infrared imager has 10 infrared filters, centered at wavelengths ranging from 6.78 to 14.88 μm with an average spectral bandwidth of 1 μm (Christensen et al., 2004). To determine the actual surface kinetic temperatures from a THEMIS infrared radiance image, one needs to know the spectral emissivity of the surface at that wavelength, and account for atmospheric emission and attenuation by dust or ice clouds. Smith et al. (2003) have calculated the relative spectral response of each THEMIS IR band to the presence of atmospheric dust and ice particles, and developed an algorithm for deriving optical depth. Their results indicate that Band 9 is very sensitive to ice clouds, Band 5 is most sensitive to dust clouds, and Band 3 is least sensitive to both cloud types. Band 3 is also centered at a wavelength (7.93 μm) where most rock-forming minerals have a near-unity emissivity. Therefore our approach was, for daytime images, to assume Band 3 brightness temperatures were equal to the surface kinetic temperatures, as long as both Bands 5 and 9 indicated low aerosol optical depths ($\tau_{IR} < 0.30$). Because nighttime images usually contain only Bands 4, 5, and 9, we used the daytime image ratio of Band 4 to Band 3 to estimate the surface emissivity and applied that to Band 4 to derive the kinetic temperature. As an example of the data, Fig. A.2 shows the calculated daytime and nighttime surface temperatures (T_{am} and T_{pm}) for a region containing LLO 'B.' Low thermal inertia surfaces, such as dust, get warmer during the day and colder at night compared to high thermal inertia surfaces, such as rock. Thus, these temperature images only provide qualitative information: LLO 'B' is a high thermal inertia unit, surrounded by relatively low thermal inertia material.

Our procedure for deriving a thermal inertia map involves finding one or more daytime and nighttime pairs of THEMIS IR images that overlap in the region of interest, and using the pairs to derive values for both the thermal inertia and the albedo simultaneously. First, we use USGS Integrated Software for Imagers and Spectrometers (ISIS) programs to extract the map-projected images for the bands of interest. We then import images into MATLAB as matrices, convert the radiance values to surface temperatures (as described above) and, using the map-projection parameters generated by ISIS, create corresponding matrices containing the latitude and longitude of each pixel. We also import relevant MOLA 128 pixel degree^{-1} topographic data. Choosing one of the temperature latitude/longitude grids to be the "master grid," we interpolate the other temperature and topography matrices to obtain values, at each master gridpoint, for all of the relevant quantities: T_{am}, T_{pm}, θ, and φ. Finally, we used the thermal model to create look-up tables of surface temperatures at the season and time of day corresponding to each THEMIS image (T_{am} and T_{pm}), as a function of solar albedo (A), thermal inertia (TI), θ, and φ. Then the best-fit values of thermal inertia and albedo are determined by least-squares analysis, i.e., these quantities are fitted to the observed day and night surface temperatures for the particular place on Mars at the orbital positions and local times of the available daytime/nighttime pairs of THEMIS images.

The sources of uncertainty in our derived values can be divided into two categories: model input and model processes. The uncertainty in the input data includes noise in THEMIS

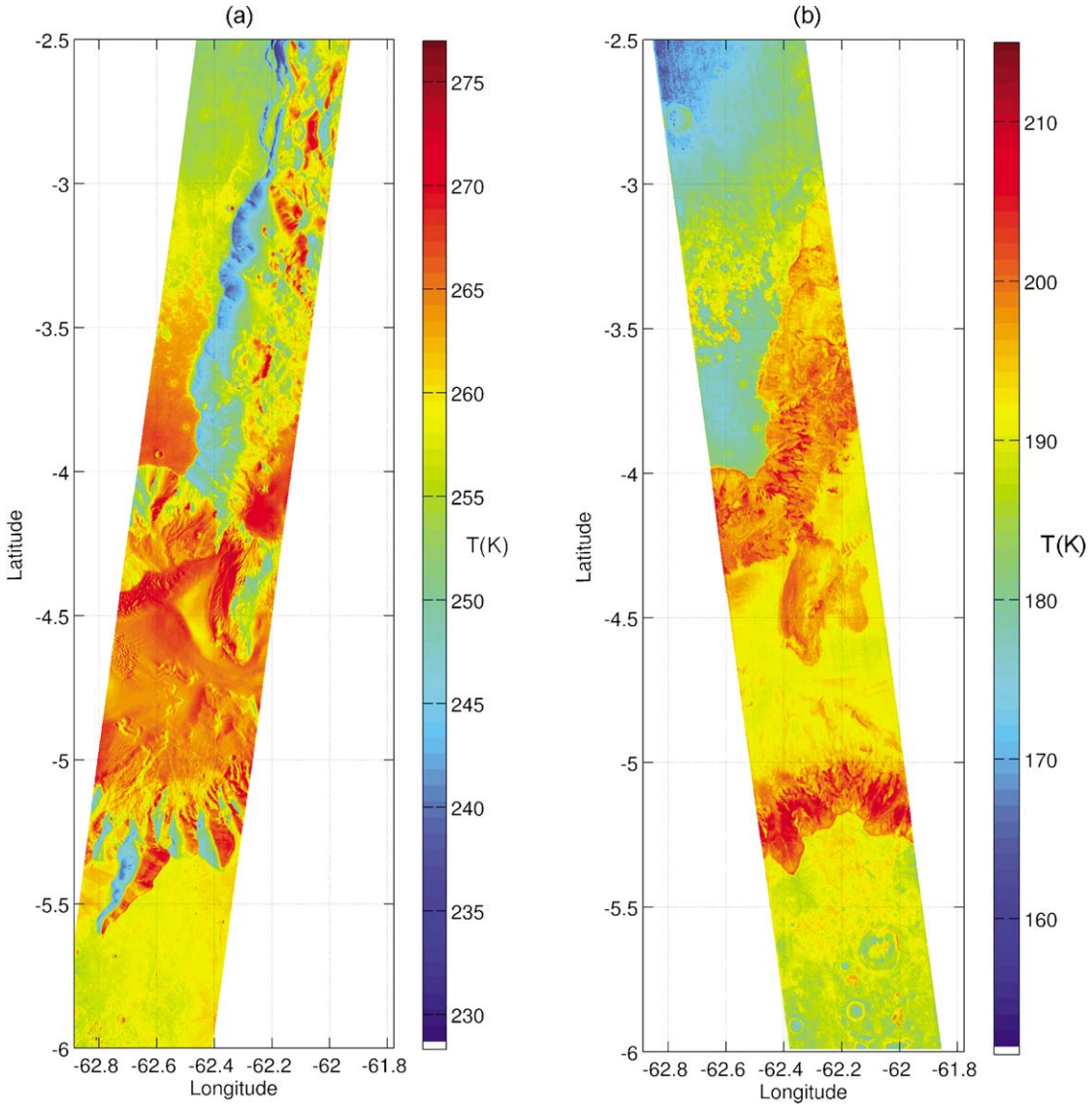

Fig. A.2. (a) Daytime and (b) nighttime THEMIS IR brightness temperature images of LLO 'B' (centered at 4.4° S, 62.3° W) and surrounding region.

brightness temperatures, e.g., ∼0.5 K at 245 K and ∼1.0 K at 180 K (supplementary data to Christensen et al., 2003). In addition, there is uncertainty in deriving model input parameters from input data, including the actual surface temperatures (0–3 K for $\tau_{IR} < 0.3$) and interpolated slope and azimuth angles due to fourfold differences in horizontal resolution of MOLA and THEMIS. The nominal model does not include reduction of direct insolation by dust/ice clouds, increase of diffuse sky illumination by dust/ice clouds, radiative flux between surfaces (reflected solar and emitted thermal), or topographic shadowing. Considering only the uncertainties associated with model input temperatures, we found that a 1 K change in the daytime temperature would change our best-fit albedo by ∼0.01, and a 1 K change in the nighttime temperature would change the thermal inertia by $\sim 20\ \mathrm{J\,m^{-2}\,s^{-1/2}\,K^{-1}}$. The error associated with processes that are not included is much harder to quantify, but most of the ones listed above are primarily, or exclusively, daytime factors, and would therefore mainly affect albedo values. We have performed a limited case study—discussed below—which shows that including some of these effects does tend to decrease our derived albedo values quite significantly—actually bringing them more in line with the TES observations, while the thermal inertia values remain much the same.

A.2. Validation

Our TI results are much higher spatial resolution than previously derived thermal inertias from TES data (Mellon et al., 2000). However, we can validate our results against TES by examining sufficient large areas in THEMIS images (>9 $\mathrm{km^2}$) that appear to be relatively homogeneous geologic units. For example, a sand sheet exists in the southern part of Juventae Chasma. From THEMIS data, we calculated the sand sheet to have a typical thermal inertia of $\sim 350\ \mathrm{J\,m^{-2}\,s^{-1/2}\,K^{-1}}$. The corresponding TES-derived thermal inertia value from the map of Mellon et al. (2000) is $\sim 340\ \mathrm{J\,m^{-2}\,s^{-1/2}\,K^{-1}}$. Similarly, we found the Hesperian plain to the west of Juventae Chasma has a typical thermal inertia of $\sim 290\ \mathrm{J\,m^{-2}\,s^{-1/2}\,K^{-1}}$, matching the

TES thermal inertia in this region of 250–300 J m^{-2} s$^{-1/2}$ K^{-1}. Albedos derived from thermal models have traditionally been found to be higher than bolometric albedos (Mellon et al., 2000). For the typical interior of the Juventae Chasma sand sheet, our thermally derived albedos from THEMIS data range from 0.20–0.26, which compares with a TES bolometer albedo of ∼0.15. For the Hesperian plateau adjacent to the chasm, we calculated ∼0.26, compared to ∼0.17 from TES. In an effort to explain these rather large discrepancies, we used an algorithm similar to the one described in Smith et al. (2003) to derive the infrared atmospheric optical depths (τ_{IR}) of dust and ice for THEMIS image I01450007 (Fig. A.2a). We found that for areas inside the Chasma $\tau_{dust,IR} = 0.17 \pm 0.02$ and $\tau_{ice,IR} = 0.01 \pm 0.002$ (in Band 5, centered at 9.35 μm), and surface temperatures (T_s) were ∼2.5 K higher than the Band 3 brightness temperatures (T_{B3}). For areas on the surrounding plateau, $\tau_{dust,IR} = 0.13 \pm 0.02$, $\tau_{ice,IR} = 0.01 \pm 0.002$, and $T_s - T_{B3} \cong 1.5$ K, where a smaller dust optical depth would be expected due to its much higher elevation. Choosing a flat location on the Chasma floor sand sheet, we found that increasing the observed surface temperature by 2.5 K reduced the best-fit albedo from 0.24 to 0.21. However, if we also included the radiative effects of dust on the incoming solar radiation in a single-point thermal model, using a parameterization from Pollack et al. (1990) and assuming that the ratio of visible to infrared optical depths is ∼2 (Clancy et al., 2003), the total insolation (direct plus diffuse) is reduced by 12%, and the best-fit albedo at this location drops to 0.12. This albedo is identical to the TES bolometer value, while the best-fit thermal inertia changes very little (320 to 330 J m^{-2} s$^{-1/2}$ K^{-1}).

Appendix B. Anhydrite–gypsum stability

For any chemical reaction, the Gibbs free energy change of the reaction ΔG, at absolute temperature T is related to the Gibbs free energy change of the reaction under standard conditions ΔG^0, by

$$\Delta G = \Delta G^0 + RT \ln Q, \tag{B.1}$$

where Q is the reaction quotient (equal to the equilibrium constant if all substances are in their standard state) and R is the ideal gas constant. For Eq. (1), the gypsum–anhydrite stability reaction, the reaction quotient is

$$Q = \frac{a_{\text{anhydrite}}(a_{H_2O})^2}{a_{\text{gypsum}}}, \tag{B.2}$$

where $a_{\text{anhydrite}}$, a_{H_2O}, and a_{gypsum} are the activities of anhydrite, water, and gypsum, respectively. At 1 bar, gypsum and anhydrite are in their standard states and $a_{\text{anhydrite}} = 1$ and $a_{\text{gypsum}} = 1$, so that Eq. (B.2) simplifies to $Q = (a_{H_2O})^2$. We will assume 1 bar pressure for our calculations because the pressure-dependence of the thermodynamics is minor compared to the temperature-dependence in the likely pressure regime for water on early Mars. (The gypsum–anhydrite transition temperature decreases about 1 °C per 40-bar pressure increase.) Consequently, Eq. (B.1) simplifies to

$$\Delta G = \Delta G^0 + 2RT \ln a_{H_2O}. \tag{B.3}$$

At equilibrium, the free energy change of reaction is given by $\Delta G = 0$. Hence, at equilibrium,

$$\Delta G^0 + 2RT \ln a_{H_2O} = 0. \tag{B.4}$$

If we know the temperature dependence of ΔG^0, we can numerically solve Eq. (B.4) for temperature T, which is the temperature for equilibrium between gypsum and anhydrite. Raju and Atkinson (1990) provide thermodynamic data, giving

$$\Delta G^0 = -74.132T \ln T + 0.10276\frac{T^2}{2} - \frac{18.376 \times 10^5}{2T} + 5715 + 403.15T. \tag{B.5}$$

Here, we have corrected the last term in T from an equation given by Raju and Atkinson (1990) that is apparently in error, noting an inconsistency with their tabulated thermodynamic data (Table 2 of Raju and Atkinson, 1990). Substituting for (B.5), solution of Eq. (B.4) for T gives the plot shown in Fig. 21.

References

Armstrong, J.C., Leovy, C.B., Quinn, T., 2004. A 1 Gyr climate model for Mars: New orbital statistics and the importance of seasonally resolved polar processes. Icarus 171, 255–271.

Baker, V.R., Kochel, R.C., 1979. Martian channel morphology—Maja and Kasei Valles. J. Geophys. Res. 84, 7961–7983.

Bibring, J.P., Langevin, Y., Gendrin, A., Gondet, B., Poulet, F., Berthe, M., Soufflot, A., Arvidson, R., Mangold, N., Mustard, J., Drossart, P., Omega-Team, O., 2005. Mars surface diversity as revealed by the OMEGA/Mars Express observations. Science 307, 1576–1581.

Bucher, W.H., 1932. "Strath" as a geomorphic term. Science, 130–132.

Carslaw, H.S.J.J.C., 1959. Conduction of Heat in Solids. Oxford Univ. Press, London.

Catling, D.C., Moore, J.M., 2003. The nature of coarse-grained crystalline hematite and its implications for the early environment of Mars. Icarus 165, 277–300.

Chapman, M.G., Tanaka, K.L., 2001. The interior deposits on Mars: Sub-ice volcanoes? J. Geophys. Res. 106, 10087–10100.

Chapman, M.G., Gudmundsson, M.T., Russell, A.J., Hare, T.M., 2003. Possible Juventae Chasma sub-ice volcanic eruptions and Maja Valles ice outburst floods on Mars: Implications of Mars Global Surveyor crater densities, geomorphology, and topography. J. Geophys. Res. 108, doi:10.1029/2002JE002009. 5113.

Christensen, P.R., Anderson, D.L., Chase, S.C., Clark, R.N., Kieffer, H.H., Malin, M.C., Pearl, J.C., Carpenter, J., Bandiera, N., Brown, F.G., Silverman, S., 1992. Thermal Emission Spectrometer experiment: Mars Observer mission. J. Geophys. Res. 97, 7719–7734.

Christensen, P.R., Anderson, D.L., Chase, S.C., Clancy, R.T., Clark, R.N., Conrath, B.J., Kieffer, H.H., Kuzmin, R.O., Malin, M.C., Pearl, J.C., Roush, T.L., Smith, M.D., 1998. Results from the Mars Global Surveyor Thermal Emission Spectrometer. Science 279, 1692–1698.

Christensen, P.R., Bandfield, J.L., Bell, J.F., Gorelick, N., Hamilton, V.E., Ivanov, A., Jakosky, B.M., Kieffer, H.H., Lane, M.D., Jakosky, B.M., Kieffer, H.H., Lane, M.D., Malin, M.C., McConnochie, T., McEwen, A.S., McSween, H.Y., Mehall, G.L., Moersch, J.E., Nealson, K.H., Rice, J.W., Richardson, M.I., Ruff, S.W., Smith, M.D., Titus, T.N., Wyatt, M.B., 2003. Morphology and composition of the surface of Mars: Mars Odyssey THEMIS results. Science 300, 2056–2061.

Christensen, P.R., Jakosky, B., Kieffer, H.H., Malin, M.C., McSween, H.Y., Nealson, K., Mehall, G.L., Silverman, S.H., Ferry, S., Caplinger, M., Ravine, M., 2004. The Thermal Emission Imaging System (THEMIS) for the Mars 2001 Odyssey mission. Space Sci. Rev. 110, 85–130.

Clancy, R.T., Wolff, M.J., Christensen, P.R., 2003. Mars aerosol studies with the MGS TES Emission phase function observations: Optical depths, particle sizes, and ice cloud types versus latitude and solar longitude. J. Geophys. Res. 108. 5098.

D'Ans, J., 1968. Der Ubergangspunkt Gips–Anhydrit. Kali Steinsalz 6, 109–111.

Farquhar, J., Savarino, J., Jackson, T.L., Thiemans, M.H., 2000. Evidence of atmospheric sulfur in the martian regolith from sulfur isotopes in meteorites. Nature 404, 50–52.

Gendrin, A., Mangold, N., Bibring, J.P., Langevin, Y., Gondet, B., Poulet, F., Bonello, G., Quantin, C., Mustard, J., Arvidson, R., LeMouelic, S., 2005. Sulfates in martian layered terrains: The OMEGA/Mars Express view. Science 307, 1587–1591.

Haberle, R.M., Jakosky, B.M., 1991. Atmospheric effects on the remote determination of thermal inertia on Mars. Icarus 90, 187–204.

Haberle, R.M., Murphy, J.R., Schaeffer, J., 2003. Orbital change experiments with a Mars general circulation model. Icarus 161, 66–89.

Hardie, L.A., 1967. Gypsum–anhydrite equilibrium at one atmosphere pressure. Am. Mineral. 52, 171–200.

Hartmann, W.K., Neukum, G., 2001. Cratering chronology and the evolution of Mars. Space Sci. Rev. 96, 165–194.

Herkenhoff, K.E., Plaut, J.J., 2000. Surface ages and resurfacing rates of the polar layered deposits on Mars. Icarus 144, 243–253.

Herkenhoff, K.E., Squyres, S.W., Arvidson, R., Bass, D.S., Bell, J.F., Bertelsen, P., Ehlmann, B.L., Farrand, W., Gaddis, L., Greeley, R., Grotzinger, J., Hayes, A.G., Hviid, S.F., Johnson, J.R., Jolliff, B., Kinch, K.M., Knoll, A.H., Madsen, M.B., Maki, J.N., McLennan, S.M., McSween, H.Y., Ming, D.W., Rice, J.W., Richter, L., Sims, M., Smith, P.H., Soderblom, L.A., Spanovich, N., Sullivan, R., Thompson, S., Wdowiak, T., Weitz, C., Whelley, P., 2004. Evidence from Opportunity's microscopic imager for water on Meridiani Planum. Science 306, 1727–1730.

Kieffer, H.H., Martin, T.Z., Peterfreund, A.R., Jakosky, B.M., Miner, E.D., Palluconi, F.D., 1977. Thermal and albedo mapping of Mars during the Viking primary mission. J. Geophys. Res. 82, 4249–4291.

Knacke, O., Gans, W., 1977. Thermodynamics of system $CaSO_4$–H_2O. Z. Phys. Chem. 104, 41–48.

Komar, P.D., 1979. Comparison of the hydraulics of water flows in martian outflow channels with flows of similar scale on Earth. Icarus 37, 156–181.

Komatsu, G., Geissler, P.E., Strom, R.G., Singer, R.B., 1993. Stratigraphy and erosional landforms of layered deposits in Valles Marineris, Mars. J. Geophys. Res. 98, 11105–11121.

Komatsu, G., Ori, G.G., Paolo, C., Litasov, Y.D., 2004. Interior layered deposits of Valles Marineris, Mars: Analogous sub-ice volcanism related to Baikal rifting, southern Siberia. Planet. Space Sci. 52, 167–187.

Laskar, J., Correia, A.C.M., Gastineau, M., Joutel, F., Levrard, B., Robutel, P., 2004. Long term evolution and chaotic diffusion of the insolation quantities of Mars. Icarus 170, 343–364.

Lucchitta, B.K., 2001. MOC images confirm layered deposits formed within Valles Marineris, Mars. Lunar Planet. Sci. XXXII, 1359. Abstract.

Lucchitta, B.K., Isbell, N.K., Howingtonkraus, A., 1994. Topography of Valles Marineris—Implications for erosional and structural history. J. Geophys. Res. 99, 3783–3798.

Malin, M.C., 1976. Nature and Origin of the Intercrater Plains on Mars. Ph.D. Thesis. Calif. Inst. of Technol., Pasadena, CA.

Malin, M.C., Edgett, K.S., 2000a. The geomorphic expression of north versus south polar layered outcrops on Mars at meter to decameter scales. In: Second Int. Conf. on Mars Polar Sci. and Exploration. Abstract 4042.

Malin, M.C., Edgett, K.S., 2000b. Sedimentary rocks of early Mars. Science 290, 1927–1937.

Malin, M.C., Edgett, K.S., 2001. Mars Global Surveyor Mars Orbiter Camera: Interplanetary cruise through primary mission. J. Geophys. Res. 106, 23429–23570.

McCauley, J.F., 1978. Geologic Map of the Coprates Quadrangle of Mars, scale 1:5,000,000. U.S. Geol. Surv. Misc. Inv. Series Map I-897.

McEwen, A.S., 2004. New Age Mars. Lunar Planet. Sci. XXXV, 1756. Abstract.

McKay, C.P., Nedell, S.S., 1988. Are there carbonate deposits in the Valles Marineris, Mars? Icarus 73, 142–148.

Mellon, M.T., Jakosky, B.M., 1995. The distribution and behavior of martian ground ice during past and present epochs. J. Geophys. Res. 100, 11781–11799.

Mellon, M.T., Jakosky, B.M., Kieffer, H.H., Christensen, P.R., 2000. High-resolution thermal inertia mapping from the Mars Global Surveyor Thermal Emission Spectrometer. Icarus 148, 437–455.

Michalski, G., Bohlke, J.K., Thiemens, M., 2004. Long term atmospheric deposition as the source of nitrate and other salts in the Atacama Desert, Chile: New evidence from mass-independent oxygen isotopic compositions. Geochim. Cosmochim. Acta 68, 4023–4038.

Montgomery, D.R., Gillespie, A., 2005. Formation of martian outflow channels by catastrophic dewatering of evaporite deposits. Geology 33, 625–628.

Nedell, S.S., Squyres, S.W., Andersen, D.W., 1987. Origin and evolution of the layered deposits in the Valles Marineris, Mars. Icarus 70, 409–441.

Paige, D.A., Wood, S.E., 1992. Modeling the martian seasonal CO_2 cycle. 2. Interannual variability. Icarus 99, 15–27.

Paige, D.A., Bachman, J.E., Keegan, K.D., 1994. Thermal and albedo mapping of the polar-regions of Mars using Viking Thermal Mapper observations. 1. North polar-region. J. Geophys. Res. 99, 25959–25991.

Peterson, C., 1981. A secondary origin for the central plateau of Hebes Chasma. Proc. Lunar Sci. Conf. 11, 1459–1471.

Pollack, J.B., Haberle, R.M., Schaeffer, J., Lee, H., 1990. Simulations of the general circulation of the martian atmosphere. 1. Polar processes. J. Geophys. Res. 95, 1447–1473.

Presley, M.A., Christensen, P.R., 1997. Thermal conductivity measurements of particulate materials. 2. Results. J. Geophys. Res. 102, 6551–6566.

Putzig, N.E., Mellon, M.T., Kretke, K.A., Arvidson, R.E., 2005. Global thermal inertia and surface properties of Mars from the MGS mapping mission. Icarus 173, 325–341.

Raju, K.U.G., Atkinson, G., 1990. The thermodynamics of "scale" mineral solubilities. 3. Calcium sulfate in aqueous NaCl. J. Chem. Eng. Data 35, 361–367.

Ruff, S.W., Christensen, P.R., Clark, R.N., Kieffer, H.H., Malin, M.C., Bandfield, J.L., Jakosky, B.M., Lane, M.D., Mellon, M.T., Presley, M.A., 2001. Mars' "White Rock" feature lacks evidence of an aqueous origin: Results from Mars Global Surveyor. J. Geophys. Res. 106, 23921–23928.

Schreiber, B.C., 1986. Arid shorelines and evaporites. In: Reading, H.G. (Ed.), Sedimentary Environments and Facies. Elsevier, New York, pp. 189–228.

Seinfeld, J.H., Pandis, S.N., 1998. Atmospheric Chemistry and Physics. Wiley, New York.

Settle, M., 1979. Formation and deposition of volcanic sulfate aerosols on Mars. J. Geophys. Res. 84, 8343–8354.

Sharp, R.P., 1973. Mars: Fretted and chaotic terrain. J. Geophys. Res. 78, 4073–4083.

Smith, D.E., Zuber, M.T., Frey, H.V., Garvin, J.B., Head, J.W., Muhleman, D.O., Pettengill, G.H., Phillips, R.J., Solomon, S.C., Zwally, H.J., Banerdt, W.B., Duxbury, T.C., Golombek, M.P., Lemoine, F.G., Neumann, G.A., Rowlands, D.D., Aharonson, O., Ford, P.G., Ivanov, A.B., Johnson, C.L., McGovern, P.J., Abshire, J.B., Afzal, R.S., Sun, X.L., 2001. Mars Orbiter Laser Altimeter: Experiment summary after the first year of global mapping of Mars. J. Geophys. Res. 106, 23689–23722.

Smith, M.D., Bandfield, J.L., Christensen, P.R., Richardson, M.I., 2003. Thermal Emission Imaging System (THEMIS) Infrared observations of atmospheric dust and water ice cloud optical depth. J. Geophys. Res. 108, 5115.

Spencer, J.R., Fanale, F.P., 1990. New models for the origin of Valles Marineris closed depressions. J. Geophys. Res. 95, 14301–14313.

Squyres, S.W., Arvidson, R.E., Bell, J.F., Bruckner, J., Cabrol, N.A., Calvin, W., Carr, M.H., Christensen, P.R., Clark, B.C., Crumpter, L., Des Marais, D.J., D'Uston, C., Economou, T., Farmer, J., Farrand, W., Folkner, W., Golombek, M., Gorevan, S., Grant, J.A., Greeley, R., Grotzinger, J., Haskin, L., Herkenhoff, K.E., Hviid, S., Johnson, J., Klingelhofer, G., Knoll, A.H., Landis, G., Lemmon, M., Li, R., Madsen, M.B., Malin, M.C., McLennan, S.M., McSween, H.Y., Ming, D.W., Moersch, J., Morris, R.V., Parker, T., Rice, J.W., Richter, L., Rieder, R., Sims, M., Smith, M., Smith, P., Soderblom, L.A., Sutlivan, R., Wanke, H., Wdowiak, T., Wolff, M., Yen, A., 2004a. The Opportunity Rover's Athena science investigation at Meridiani Planum, Mars. Science 306, 1698–1703.

Squyres, S.W., Grotzinger, J.P., Arvidson, R.E., Bell, J.F., Calvin, W., Christensen, P.R., Clark, B.C., Crisp, J.A., Farrand, W.H., Herkenhoff, K.E., Johnson, J.R., Klingelhofer, G., Knoll, A.H., McLennan, S.M., McSween, H.Y., Morris, R.V., Rice, J.W., Rieder, R., Soderblom, L.A., 2004b. In situ evidence for an ancient aqueous environment at Meridiani Planum, Mars. Science 306, 1709–1714.

Stevens, C.H., 1977. Was development of brackish oceans a factor in Permian extinctions? Geology 88, 133–138.

Vasavada, A.R., Paige, D.A., Wood, S.E., 1999. Near-surface temperatures on Mercury and the Moon and the stability of polar ice deposits. Icarus 141, 179–193.

Wänke, H., Dreibus, G., 1994. Chemistry and accretion history of Mars. Philos. Trans. R. Soc. London A 349, 285–293.

Weitz, C.M., Parker, T.J., Anderson, F.S., Grant, J.A., 2001. The interior layered deposits of Vallis Marineris: Layering, erosional processes, and age relationships. Lunar Planet. Sci. XXXII, 1277. Abstract.